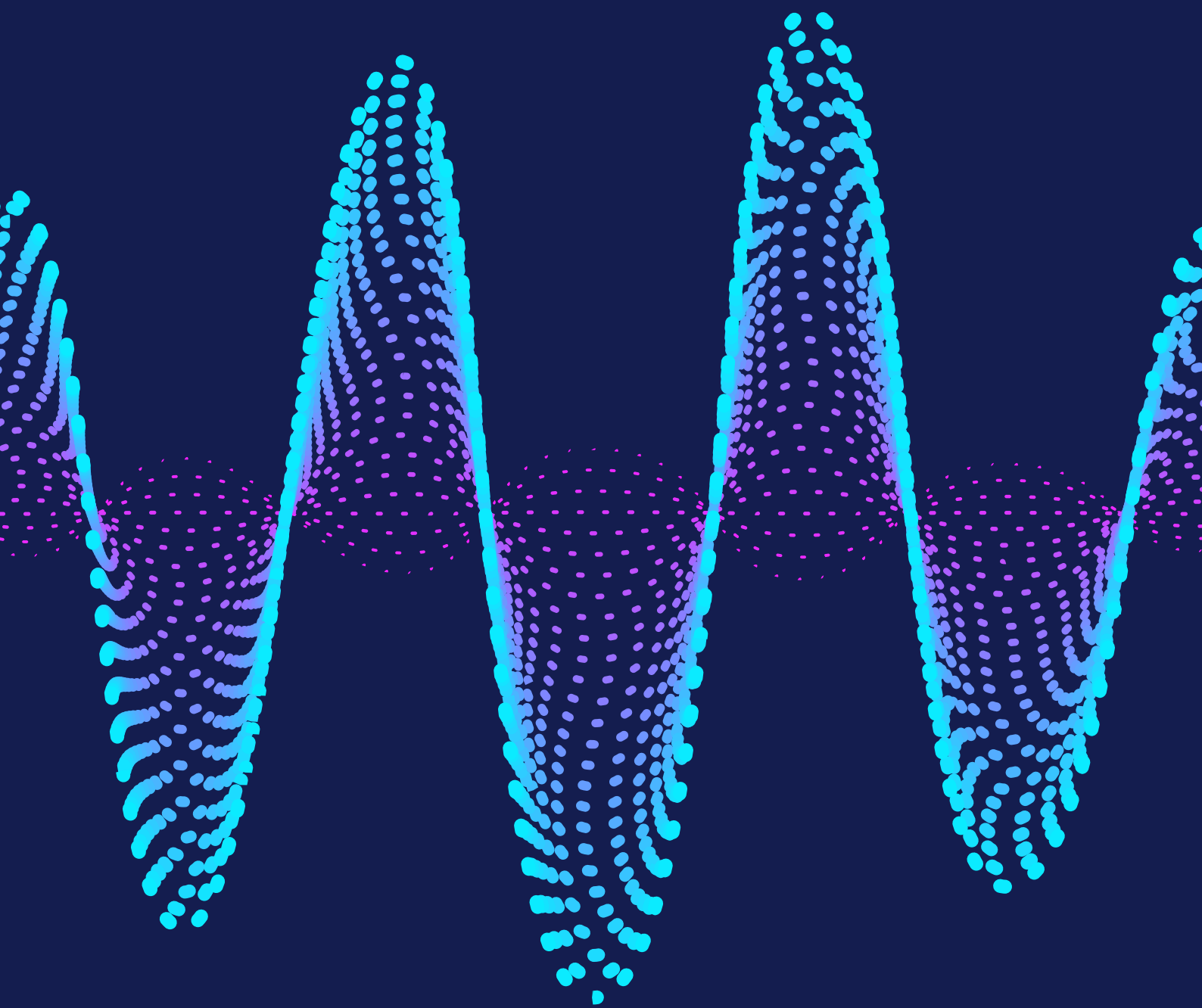


Portable Ultrasound System for Blood Velocity Estimation

Jeppe Hinrichs

Master Thesis



Portable Ultrasound System for Blood Velocity Estimation
Project Report

Master Thesis
April, 2023

Author:
Jeppe Hinrichs
Advisor(s):
Hyunjoo Lee, Xenofon Fafoutis, Tiberiu Gabriel Zsurzsan

Copyright:	Reproduction of this publication in whole, or in part, must include the customary bibliographic citation, including author attribution, report title, etc.
Cover photo:	RawPixel, 2022
Published by (1):	Technical University of Denmark, DTU Elektro, Institut for Elektroteknologi, Ørsteds Plads, Building 348, 2800 Kgs. Lyngby, Denmark www.elektro.dtu.dk
Published by (2):	Korea Advanced Institute of Science and Technology, School of Electrical Engineering, E3-2, Daehak-ro 291, 34141 Daejeon, Republic of Korea www.ee.kaist.ac.kr
Timespan:	Saturday 1 st October, 2022 ~ Wednesday 12 th April, 2023
Credits:	30 ECTS / 9 credits
Degree:	Master of Science
Field:	Electrical Engineering

Contents

Copyright	I
Contents	II
List of Figures	IV
List of Tables	VI
List of Source Codes	VII
Acronyms	VIII
Glossary	X
Reading comprehension	XI
1 Introduction	1
1.1 Literature review	1
1.2 Project scope	3
2 Theory	5
2.1 Ultrasound	5
2.1.1 Scattering	6
2.1.2 Attenuation	7
2.1.3 Transducer	8
2.1.4 Doppler effect	8
2.2 Flow Physics	10
2.2.1 Blood flow	12
2.3 Transducer	13
2.3.1 Impedance matching	15
2.4 Devices	15
2.4.1 Continuous-wave Flowmeter	17
2.4.2 Pulsed-wave Flowmeter	19
2.5 Blood Velocity Estimation	21
2.5.1 Spectral Envelope	21
2.5.2 One-Dimensional Velocity Estimation	24
2.5.3 Sonography	24
3 Synthesis	27
3.1 Control System	27
3.1.1 Development Environment	28
3.1.2 Zephyr	29
3.2 Pulse Generator	33
3.3 Power Stage	33
3.4 Transmit/Receive Switch	36
3.5 Band-Pass Filter	37
3.6 Preamplifier	38

3.7	Quadrature Demodulator	39
3.8	Sample and Hold	40
3.9	Pulse-Repetition, Wall Filter, DC-Coupling	42
4	Production	45
4.1	Control System	45
4.2	Power Stage	45
4.3	Transmit/Receive Switch	46
4.4	Band-Pass Filter	48
4.5	Preamplifier	48
4.6	Quadrature Demodulator	49
4.7	Sample and Hold	49
4.8	Pulse-Repetition and Wall Filter	52
4.9	Digital Signal Processor	52
5	Conclusion	53
5.1	Future Work	53
Bibliography		55
A Source Code		60
B Simulation Models		61
C Instruments		63

List of Figures

2.1	Particle displacement for a propagating ultrasound wave	5
2.2	Single element ultrasound transducer construction	8
2.3	Transducer types for acquiring B-mode images	9
2.4	Doppler effect diagram	9
2.5	Circulatory system of the human body	11
2.6	Basic CMUT structure	14
2.7	Optical images of various cMUT elements with different membrane shapes .	15
2.8	Diagram of ultrasound wave transmitted and reaching blood vessel with incident angle θ	16
2.9	Block diagram of continuous-wave flowmeter	16
2.10	Demodulation effects of Doppler signals in time and frequency domain . .	18
2.11	Block diagram of pulsed-wave flowmeter	19
2.12	Sampling for a gate pulsed wave system with a single range	20
2.13	Simulated RF sampling of blood vessel with segmented receiver line with a sample interval denoted by a dotted line (left) and the resulting amplitude of the sample (right) [32]	21
2.14	Stationary tissue sampled signal and stationary tissue sample spectrum .	22
2.15	Single moving scatterer crossing a concave transducer beam	23
2.16	Frequency axis scaling for scatterer with velocity v_z	23
2.17	Arterial sonogram with time-frequency and Doppler shift	25
3.1	Simplified overview of the entire system	27
3.2	VSCode editor with CMake Tools active	28
3.3	Devicetree input files and output files	29
3.4	Configuration phase of a Zephyr application	30
3.5	Flowchart of build stage I, pre-build	31
3.6	Flowchart of build stage II, generation and compilation	31
3.7	Flowchart of build stage III, intermediate binary	32
3.8	Flowchart of build stage IV, second intermediate binary	32
3.9	Flowchart of build stage V, final binary	32
3.10	Flowchart of build stage VI, post-processing	33
3.11	Timing diagram of various control signals for an arbitrary n length pulse chain expressed by the second diagram gap	34
3.12	Block diagram of power stage [36]	34
3.13	LTspice simulation output of transmitter with level shifter and half-bridge power stage from fig. B.1	35
3.14	Block diagram of TX/RX switching circuit where the inputs D1 through D6 are binary decoded from inputs B_1, B_2, B_3 [25]	36
3.15	Timing diagram of switching interface	36
3.16	3D Render of PCB in Altium Designer	37
3.17	Band-Pass Filter insertion loss and specifications	38
3.18	Block diagram of preamplifier AD8332 [41]	38
3.19	LTspice simulation output of preamplifier low noise amplifier (<i>LNA</i>) and variable gain amplifier (<i>VGA</i>) from fig. B.2	39
3.20	Block diagram of demodulator AD8333 [42]	39
3.21	LTspice simulation demodulator input variables from fig. B.3	40

3.22 LTspice simulation demodulator output variables Q and I voltages from fig. B.3	41
3.23 AD783 Sample and Hold Amplifier functional block diagram [34]	41
3.24 Sample and Hold function with input function $f(t)$ over time [62]	42
3.25 Small-signal analysis of DC-Coupling filter circuit	43
3.26 Transient analysis of DC-Coupling filter circuit	43
4.1 MD1213DB1 High Speed Pulser	45
4.2 Measured input and output of power stage PCB	46
4.3 Transmit/Receive Switch after assembly	46
4.4 TX/RX Switch reflection experiment with water tank	47
4.5 Measured transmit and receive on Transmit/Receive Switch PCB	48
4.6 Band-pass filter bode plot	49
4.7 Measured input and output of preamplifier PCB	50
4.8 Demodulator PCB AD8333-EVALZ	50
4.9 Measured input of demodulator PCB	51
4.10 Measured output of demodulator PCB	51
4.11 Measured input and output of Sample and Hold amplifier	52
B.1 LTspice model of transmitter	61
B.2 LTspice model of preamplifier	61
B.3 LTspice model of demodulator	62
B.4 LTspice model of DC Coupler	62

List of Tables

1.1	Comparison of medical imaging modalities	2
1.2	Project specification	3
2.1	Approximate density, sound speed, and acoustic impedance of human tissue types	6
2.2	Approximate attenuation values for human tissue	7
2.3	Typical dimensions and flow in human circulatory system	13
2.4	Measured frequency shifts with a Doppler 3 MHz transducer at various velocities at a 45° incident angle	18
C.1	List of instruments used for solder work	63
C.2	List of instruments used in experiments	63

List of Source Codes

Acronyms

Notation	Description
<i>ADC</i>	analogue-to-digital converter
<i>AFE</i>	analogue front end
<i>ASIC</i>	application-specific integrated circuit
<i>BLE</i>	bluetooth low energy
<i>BP</i>	band-pass
<i>CMUT</i>	capacitive micromachined ultrasound transducer
<i>CPU</i>	central processing unit
<i>CT</i>	computed tomography
<i>CVD</i>	cardiovascular diseases
<i>CW</i>	continuous-wave
<i>DSP</i>	digital signal processor
<i>DTS</i>	device tree source
<i>DTSI</i>	device tree source include
<i>DTU</i>	Danmarks Tekniske Universitet (Technical University of Denmark)
<i>ELF</i>	executable and linkable format
<i>FET</i>	field-effect transistor
<i>FPGA</i>	field-programmable gate array
<i>HP</i>	high-pass
<i>I/O</i>	input/output
<i>IC</i>	integrated circuit
<i>IoT</i>	Internet of Things
<i>KAIST</i>	Korea Advanced Institute of Science and Technology
<i>LNA</i>	low noise amplifier
<i>low-res</i>	low resolution
<i>LSB</i>	least significant bit
<i>MCU</i>	microcontroller unit
<i>MOSFET</i>	metal-oxide-semiconductor field-effect transistor
<i>MRI</i>	magnetic resonance imaging
<i>PRF</i>	pulse repetition frequency
<i>PSD</i>	power spectral density
<i>PW</i>	pulsed-wave

Notation	Description
PZT	lead circonate titanate
RAM	random access memory
$RTOS$	real-time operating system
SoC	system-on-a-chip
US	ultrasound
VGA	variable gain amplifier
VNA	vector network analyzer

Glossary

Notation	Description
adiabatic	Any process that happens without heat gain or loss is considered adiabatic
Doppler effect	A change in frequency of a wave in relation to an observer who is moving relative to the wave source
flashing	Refers to the process of programming the non-volatile memory of a microcontroller
HIGH	Logic high voltage level
Internet of Things	A term used to describe physical things equipped with sensors, computing power, software, and other technologies that communicate data with other systems and devices across communication networks such as the Internet
LOW	Logic low voltage level
monochromatic wave	A wave which has only a single frequency
open-source	Refers to software whose original source code is publicly available and may be changed and distributed
piezoelectric	Material that deforms under electric excitation, or reversibly, electric charge that accumulates in response to mechanical stress
SPICE	SPICE ("Simulation Program with Integrated Circuit Emphasis") is an open-source IC and board-level circuit simulator
transcutaneous	Applied across the depth of the skin without invasive penetration
transducer	A device that converts electrical energy to kinetic energy, or kinetic energy to electrical energy

Reading comprehension

This section of the report will explain to the reader how to reference this document and explain the fundamental structure of the project as well as the report. It is assumed that the reader has a basic knowledge of physics, electrical engineering, computing, and circuit analysis.

Otherwise, please refer to Abbreviations, Glossary, and Nomenclature pages for explanations to terms found within the report.

Sources

Calculus expressions present in the report will typically have a reference explaining their origin. All references are prominently displayed with square brackets and a number, directing to the bibliography section of the report.

1 Introduction

The progress of diagnostic imaging has advanced significantly during the 20th century. As the cost of high-speed computational systems has grown increasingly accessible, so has the use of medical imaging become prominent. Potentially millions of people have been spared painful exploratory surgery through non-invasive diagnostic imaging. And thus, lives can be saved by early diagnosis and intervention through medical imaging. Advancements in scientific visualisation have in turn generated more complex datasets of increased size and quality. The four major technologies used are ultrasound (*US*), X-ray, computed tomography (*CT*), and magnetic resonance imaging (*MRI*). Each technology has distinct advantages and disadvantages in biomedical imaging, and thus each is still relevant for modern medicine. Table 1.1 contains a comparison and summary of the various fundamental diagnostic imaging modalities.

Since 2004, medical imaging has been reported to have been performed more than 5 billion times [16], and later numbers from 2011 show a general doubling and in particular, a tenfold increase in ultrasound examinations between 2000 and 2011 [38]. Recent data reveal that this trend of doubling has continued throughout the years 2010 to 2020 [54], and reveal that even though patient processes were disrupted during the global SARS-CoV-2 pandemic, the number of medical imaging examinations per 1000 patients still increased. The reasons for this and, particularly, why ultrasound has seen a significant increase in use, can be attributed to its high, but inconsistent, resolution, cost-effectiveness, portability, and real-time interventional imaging. The downside of ultrasound is its limited penetration and restrictions for use in certain body parts. When comparing soft tissue examinations, which ultrasound is limited to, both *CT* and *MRI* can image the entire body with consistent resolution and contrast, but are more expensive and have poor portability due to the immense size of their hardware.

The cardiovascular system, which transports oxygen and nutrients to tissue, produces a complex flow pattern that causes velocity fluctuations. Several cardiovascular diseases (*CVD*) are also known to cause abnormal blood flow. In studies published by Center for Disease Control, a person dies from CVD every 34 seconds in the United States and complications from CVD caused 229 billion USD between 2017 and 2018 [55]. As mentioned above, ultrasound is a powerful tool for performing non-invasive imaging of the cardiovascular system [26], [32], and has no adverse risk to patients. Determining power spectral density (*PSD*) of a received signal is a common way to estimate blood velocity. A processed image of *PSD* over time is commonly known as a sonogram, where changes in blood velocity over time can be seen.

1.1 Literature review

A systematic review was conducted using the PubMed, Google Scholar, Elsevier, DTU FindIt and IEEE Xplore with the search terms “pulsed-wave Doppler ultrasound”, “blood velocity estimation”, and “ultrasound flow-meter”. The search was limited to English language articles. The literature search yielded more than 50 papers, of which 37 were included [1]–[4], [6]–[14], [17], [19], [21]–[24], [27]–[31], [35], [37], [40], [43], [44], [46], [48]–[50], [52], [54], [57], [61]. In addition, textbooks [32], [38], [39] was used in the preparation and study of the theoretical principles of biomedical imaging and ultrasound.

Table 1.1: Comparison of medical imaging modalities [38]

Modality	Ultrasound	X-ray	CT	MRI
Topic	Longitudinal, shear, mechanical properties	Mean X-ray tissue absorption	Local tissue X-ray absorbtion	Biochemistry (T_1 and T_2)
Access	Small windows adequate	2 sides needed	Circumferential around body	Circumferential around body
Spatial resolution	0.2 mm to 3 mm ^a	~ 1 mm	~ 1 mm	~ 1 mm
Penetration	3 cm to 25 cm ^b	Excellent	Excellent	Excellent
Safety	Excellent	Ionizing radiation	Ionizing radiation	Very good
Speed	Real-time	Minutes	20 minutes	Varies [†]
Cost	\$	\$	\$\$	\$\$\$
Portability	Excellent	Good	Poor	Poor
Volume coverage	Real-time 3D volumes, improving	2D	Large 3D volume	Large 3D volume
Contrast	Increasing (shear)	Limited	Limited	Slightly flexible
Intervention	Real-time 3D increasing	No ^c	No	Yes, limited
Functional	Functional ultrasound	No	No	fMRI

^a Frequency and axially dependent.^b Frequency dependent.^c Fluoroscopy limited.† Typical: 45 minutes, fastest: Real-time (*low-res*).

Among these works are some of the earliest papers that outlined the field as it was emerging. Other articles study possibilities of improvements in algorithms and experimental parameters. Overall, the results indicate that the Doppler flow-meter is a reliable method for estimating blood flow velocity in various parts of the body. Studies include in-vitro and in-vivo on humans and animals alike. Some of the review articles have compared Doppler flow-meters to other imaging techniques for this application, such as magnetic resonance imaging and computed tomography angiography, and have shown that the Doppler flow-meter is a cost-effective, portable and non-invasive choice.

Based on the literature review, a gap is identified in the acquisition method of the signal chain. A number of articles study and develop the algorithms for blood flow estimation and imaging, but does not have an analogue front end (*AFE*) and use offline data acquisition methods which are not usable for clinicians. A few of the articles feature online data acquisition, but use field-programmable gate array (*FPGA*) or application-specific integrated circuit (*ASIC*) technology in the design, which are effective but less cost-effective. This high cost of parts resemble a limitation to its use. To improve the current state of ultrasound Doppler imaging there is potential to decrease cost and retain effectiveness by using modern low-cost electronics.

1.2 Project scope

Table 1.2: Project specification

Project specification
Study and research ultrasound and its principles and applications
Design and implement a device for ultrasound blood velocity estimation
Investigate and test the device in an experimental setting
Validate results with commercial equipment
Make quantifiable performance measurements on system
Write a technical report documenting the project work

Seen in table 1.2, a list of project goals are written. The project is conducted under the guidance of advisors from the affiliated institutions Danmarks Tekniske Universitet (Technical University of Denmark) (*DTU*), Department of Electrical Engineering, Department of Applied Mathematics and Computer Science, and Korea Advanced Institute of Science and Technology (*KAIST*) at the Brain/Bio Medical Microsystems Laboratory. The report is divided into five chapters, and the first part is an introduction to the project. The second chapter will focus on explaining the theory of the topic of the project. The third chapter focuses on the synthesis of a system model for experimental testing. The fourth chapter explains the method of implementation during the production of the system. The fifth chapter will explain the testing methodology performed on the hardware. Finally, additional documentation of testing, code, circuit diagrams, and laboratory setups can be found in the appendix.

2 Theory

This chapter explains the overall theory that forms the fundamental principles of this project. Initially, the characteristics of ultrasound will be explained from an acoustics standpoint. Then, a brief overview of the systemic circulation is explained *in vivo*. Lastly, the various types of flow-meters are outlined with their strengths and weaknesses.

2.1 Ultrasound

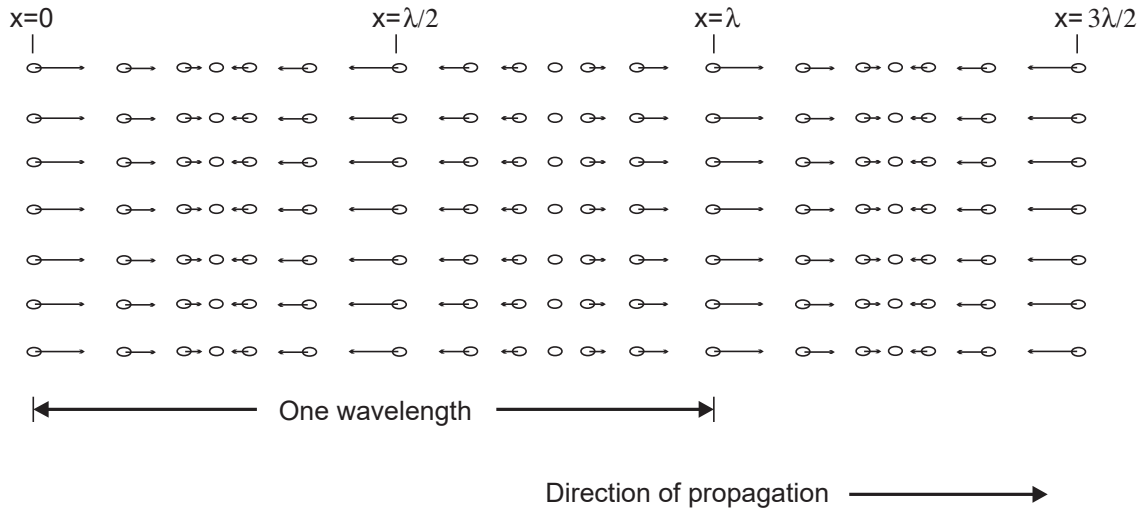


Figure 2.1: Particle displacement for a propagating ultrasound wave [32]

US is a technology that transmit sound wave with frequencies above the audible range (20 to 20 000 Hz) to mechanically vibrate matter. The particles in the medium would be at rest and distributed uniformly before any disturbance. The wave propagates as a disturbance and the particles oscillate around their mean position due to the presence of the ultrasonic wave. Typically, the *US* frequency-band used in clinical settings are from 1 to 15 MHz [38]. Certain specialist applications, such as eye, skin, and small animal imaging may use ultrasound frequencies at or above 20 MHz [31]. The trade-off with very high frequency ultrasound balances increased resolution with reduction in penetration depth. For blood velocity estimation or echocardiography, moderate penetration is more important than resolution. Thus, the frequency used is most often at 10 MHz or less. Figure 2.1 visualizes the propagation of a plane wave in matter. The oscillation occurs parallel to the wave's direction, making it longitudinal, and the disturbance will propagate with the variable c , which is determined by the medium and is given by eq. (2.1).

$$c = \sqrt{\frac{1}{\rho_0 \kappa_S}} \quad (2.1)$$

Where ρ_0 is the mean density (kgm^{-3}) and κ_S is the adiabatic compressibility (m^2N^{-1}). Since in the majority of cases, the propagation of ultrasound is linear, it is assumed in this work. The acoustic pressure of the harmonic plane wave is expressed by eq. (2.2).

$$p(t, z) = p_0 e^{j(\omega t - kz)} \quad (2.2)$$

And propagates along the z -axis. ω is the angular frequency, k is the wave number and is expressed by $k = \omega/c = 2\pi/\lambda$, and p_0 is the acoustic pressure amplitude. A spherical wave is expressed by eq. (2.3)

$$p(t, r) = p_0 e^{j(\omega t - kr)} \quad (2.3)$$

Where r is radial distance, and is defined in a polar coordinate system. For each time instance, the acoustic pressure $p(t, r)$ is constant over a fixed radial position. In this scenario, the pressure amplitude is given by $p_0(r) = k_p/r$, where k_p is a constant since the energy of the outgoing wave must be constant. Particle speed u is dependent on the pressure caused by a wave expressed by eq. (2.4)

$$u = \frac{p}{Z} \quad (2.4)$$

Where Z is the characteristic acoustic impedance, defined as the ratio of acoustic pressure to particle speed at a given position in the medium and is expressed by eq. (2.5).

$$Z = \rho_0 c \quad (2.5)$$

Characteristic acoustic impedance Z is one of the most significant variables in the characterization of propagating plane waves. Reference values for density, speed of sound, and characteristic acoustic impedance can be seen in table 2.1.

Table 2.1: Approximate density, sound speed, and acoustic impedance of human tissue types [32]

Medium	Density (ρ_0) kg/m ³	Speed of sound (c) m/s	Acoustic impedance (Z) kg/(m ² s)
Air	1.2	333	0.4×10^3
Blood	1.06×10^3	1566	1.66×10^6
Bone	$1.38\text{--}1.81 \times 10^3$	2070–5350	$3.75\text{--}7.38 \times 10^6$
Brain	1.03×10^3	1505–1612	$1.55\text{--}1.66 \times 10^6$
Fat	0.92×10^3	1446	1.33×10^6
Kidney	1.04×10^3	1567	1.62×10^6
Lung	0.4×10^3	650	0.26×10^6
Liver	1.06×10^3	1566	1.66×10^6
Muscle	1.07×10^3	1542–1626	$1.65\text{--}1.74 \times 10^6$
Spleen	1.06×10^3	1566	1.66×10^6
DI	1×10^3	1480	1.48×10^6

In the following sections, various acoustic wave phenomena will be briefly described.

2.1.1 Scattering

A wave propagating through a medium continues in the same direction until it encounters a new medium. When this occurs, a portion of the wave is transmitted into the new medium with a change in direction. Because the scattered wave is the result of several contributors, it is necessary to define it statistically. The amplitude distribution is Gaussian [32] and can thus be fully described by its mean and variance. The mean value is zero because the dispersed signal is caused by variances in the acoustic characteristics in the tissue. The

correlation between multiple data is what allows ultrasound to determine blood velocities. Because minor movements have a significant correlation, it is feasible to discover alterations in location by comparing sequential measurements of moving structures, such as blood cells. In medical ultrasound, only one transducer is used to transmit and receive, and only the backscattered signal is analysed. The power of the scattered signal is defined by the scattering cross-section, which in small cases means a uniform intensity I_i , and is expressed by eq. (2.6).

$$P_s = I_i \sigma_{sc} \quad (2.6)$$

Where σ_{sc} is the scattering cross-section in square meters. The backscattering cross section is material dependant and determines the intensity of the scattering. If the dispersed energy is evenly emitted in all directions, the scattered intensity is given by eq. (2.7).

$$I_s = \frac{P_s}{4\pi R^2} = \frac{\sigma_{sc}}{4\pi R^2} \cdot I_i \quad (2.7)$$

Where R is distance to the scattering region [32]. This results in a spherical wave. A transducer with radius r gives the power P_r , presuming the attenuation and focus is neglected, and is expressed by eq. (2.8).

$$P_r = I_s \pi r^2 = \sigma_{sc} \frac{r^2}{4R^2} \cdot I_i \quad (2.8)$$

The backscattering coefficient, which characterizes scattering from a volume of scatterers, is another measure of scattering strength. It is defined as the average received power per steradian volume of scatterers when flooded with plane waves of unit amplitude and the unit is 1/cmsr. Backscattering coefficients in the blood are significantly lower than the backscattering coefficients from various tissue types. This poses a challenge when estimating blood flow close to tissue vessel walls [5], [32].

2.1.2 Attenuation

The ultrasonic wave will be reduced as it propagates through the tissue due to absorption and scattering. The attenuation in tissue is frequency dependent, with greater attenuation with increasing frequency. Because of absorption and dispersion, the ultrasonic wave will be attenuated as it travels through the tissue. The relationship between attenuation, distance travelled, and frequency is often linear. Attenuation in the tissue occurs as a result of both dispersion, which spreads energy in all directions, and absorption, which turns it into thermal energy. A table of approximate attenuation values can be seen in table 2.2.

Table 2.2: Approximate attenuation values for human tissue [32]

Tissue	Attenuation dB/(MHz · cm)
Liver	0.6–0.9
Kidney	0.8–1
Spleen	0.5–1
Fat	1–2
Blood	0.17–0.24
Plasma	0.01
Bone	16–23

The pressure of a wave propagating in z -direction decreases exponentially expressed by eq. (2.9)

$$p(z) = p(z = 0)e^{-\alpha z} \quad (2.9)$$

Where $p(z = 0)$ is the pressure in the point of origin and α is the attenuation coefficient. The attenuation coefficient unit is Npcm^{-1} and, alternatively, dBcm^{-1} with the relationship described in eq. (2.10).

$$\alpha = \frac{1}{z} \ln \frac{p(z = 0)}{p(z)} \quad (2.10a)$$

$$\alpha(\text{dBcm}^{-1}) = 20(\log_{10} e)\alpha(\text{Npcm}^{-1}) = 8.68\alpha(\text{Npcm}^{-1}) \quad (2.10b)$$

The significance of absorption and scattering in ultrasonic attenuation in biological tissues is a point of contention. Scattering adds just a few per cent to attenuation in most soft tissues. As a result, it is fair to conclude that absorption is the primary mechanism of ultrasonic attenuation in biological tissues [39].

2.1.3 Transducer

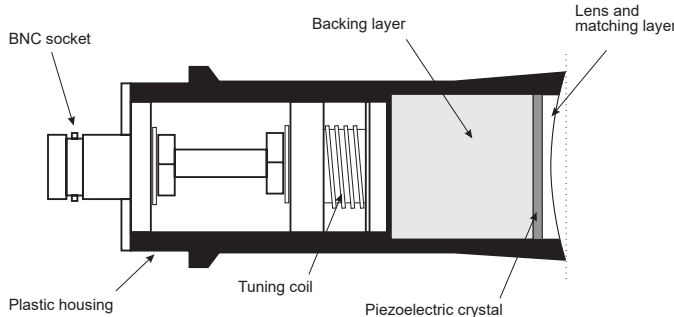


Figure 2.2: Single element ultrasound transducer construction [32]

A layperson knows transducers as speakers and microphones in the context of PA systems. In the case of medical US it is the device that generates the acoustic pressure field, which is emitted into the tissue. A common type of US transducer is a lead circonate titanate (*PZT*) type, which has a piezoelectric crystal inside the housing. When excited, this crystal emits ultrasound waves toward flowing blood. The red blood cells will reflect a fraction of the emitted waves. These reflected waves are of a different frequency than the transmitted wave. If the red blood cells move away from the transducer, the frequency will be lower. If the red blood cells are moving towards the transducer, the frequency will be higher. This is caused by the Doppler effect. The reflected ultrasonic waves return to the crystal and are converted back into electrical signals. The single-element transducer shown in fig. 2.2 has a minimal imaging window and has to be mechanically manipulated to obtain a wide window, which is unfeasible for responsive high-frequency imaging. Thus, usually, a transducer array is used. Various types of US transducer exist with different strengths and weaknesses, shown in fig. 2.3.

2.1.4 Doppler effect

The Doppler effect is a phenomenon in which an observer perceives a shift in the frequency of sound emitted from a source when either the source or the observer is moving, or both are moving. The reason for the perceived change in frequency is visualised in fig. 2.4. In diagram (a), the source S_p is stationary and produces a spherical distribution pattern of

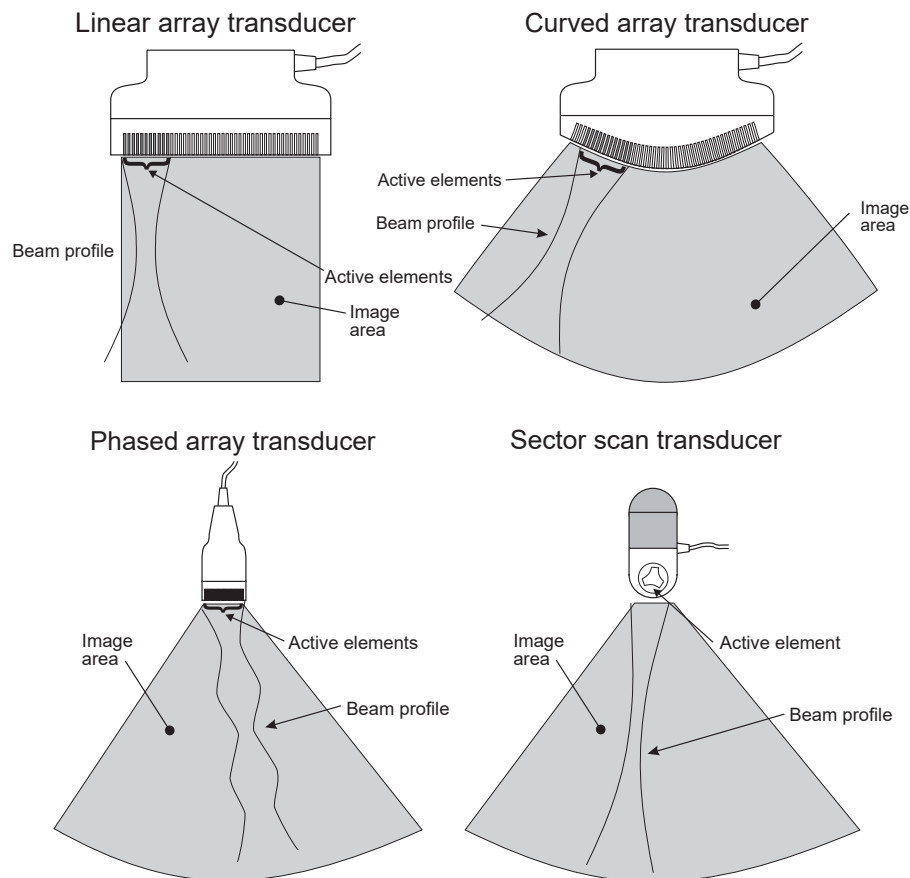


Figure 2.3: Transducer types for acquiring B-mode images [32]

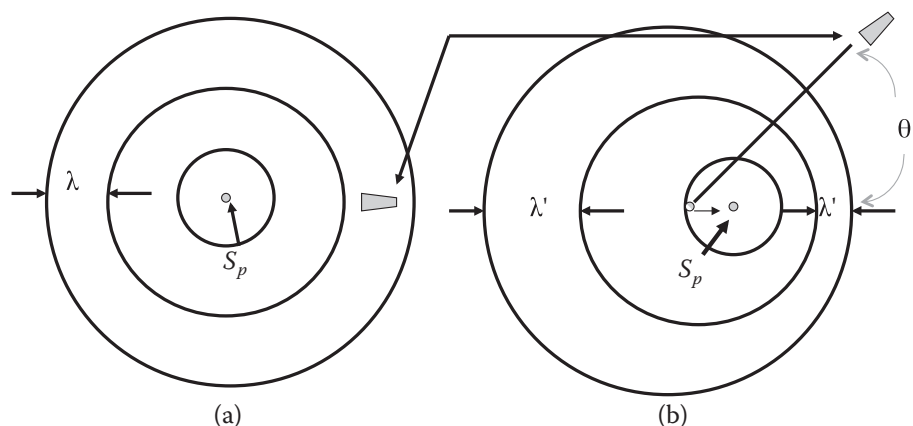


Figure 2.4: Doppler effect diagram. A stationary observer perceives a change in the frequency of a wave generated by a moving source toward the observer as a result of a wavelength shift from λ to λ' . In (a), the source is still. In (b), the source is moving at a velocity v . [39]

the wave with the perceived frequency of the observer is given by $f = c/\lambda$, where c is the velocity of the wave in the medium and λ is the wavelength. In diagram (b), the sound source is moving towards the right with a velocity v . The locomotion of the source changes the distribution pattern and causes a longer wavelength on the left, indicating a lower perceived frequency, and a shorter wavelength on the right, indicating a higher perceived frequency, both denoted as λ' in the diagram. In the case of the observer on the right side, the perceived frequency becomes eq. (2.11).

$$f' = \frac{c}{\lambda} = \frac{c}{\lambda - vT} = \frac{c}{(c - v)T} = \frac{c}{c - v} \cdot f_0 \quad (2.11)$$

And viceversa, on the left side, the perceived frequency becomes eq. (2.12).

$$f' = \frac{c}{c + v} \cdot f_0 \quad (2.12)$$

This perceived difference between the frequency that is transmitted from the source f_0 , and the perceived frequency f' is also called the Doppler frequency, f_d . When these connections are combined, the Doppler frequency for a source moving with velocity v and an observer travelling with velocity v' is given by eq. (2.13).

$$f_d = f' - f = \left(\frac{c + v'}{c - v} - 1 \right) \quad (2.13)$$

If both source and observer are moving with the same velocity, v , assuming $c \gg v$, the v cancels out and the expression is reduced to eq. (2.14).

$$f_d = \frac{2vf}{c} \quad (2.14)$$

If the velocity of the moving source is traveling with an incident angle θ , the v in eq. (2.14) is replaced with $v(\cos \theta)$. This results in the expression found in eq. (2.15) and forms the basis for applied Doppler effect measurements.

$$f_d = \frac{2v(\cos \theta)f}{c} \quad (2.15)$$

The Doppler effect is used in ultrasonic Doppler devices used to image blood flow transcutaneously. An ultrasonic transducer in these devices sends ultrasonic waves into a blood artery, and the scattered radiation from moving red cells is measured by either the same transducer or a second transducer. The Doppler frequency, which is determined by the velocity of red blood cells, is extracted using modern electronic demodulation techniques which will be explored later.

2.2 Flow Physics

The flow physics of the human circulatory system are sophisticated, and numerous non-stationary flow patterns are observed. The human circulatory system takes care of transporting oxygen and nutrients to organs, as well as disposing of waste products produced by metabolism. It is possible because the blood within the circulatory system contains several smaller sub-components, such as plasma and formed cellular elements that

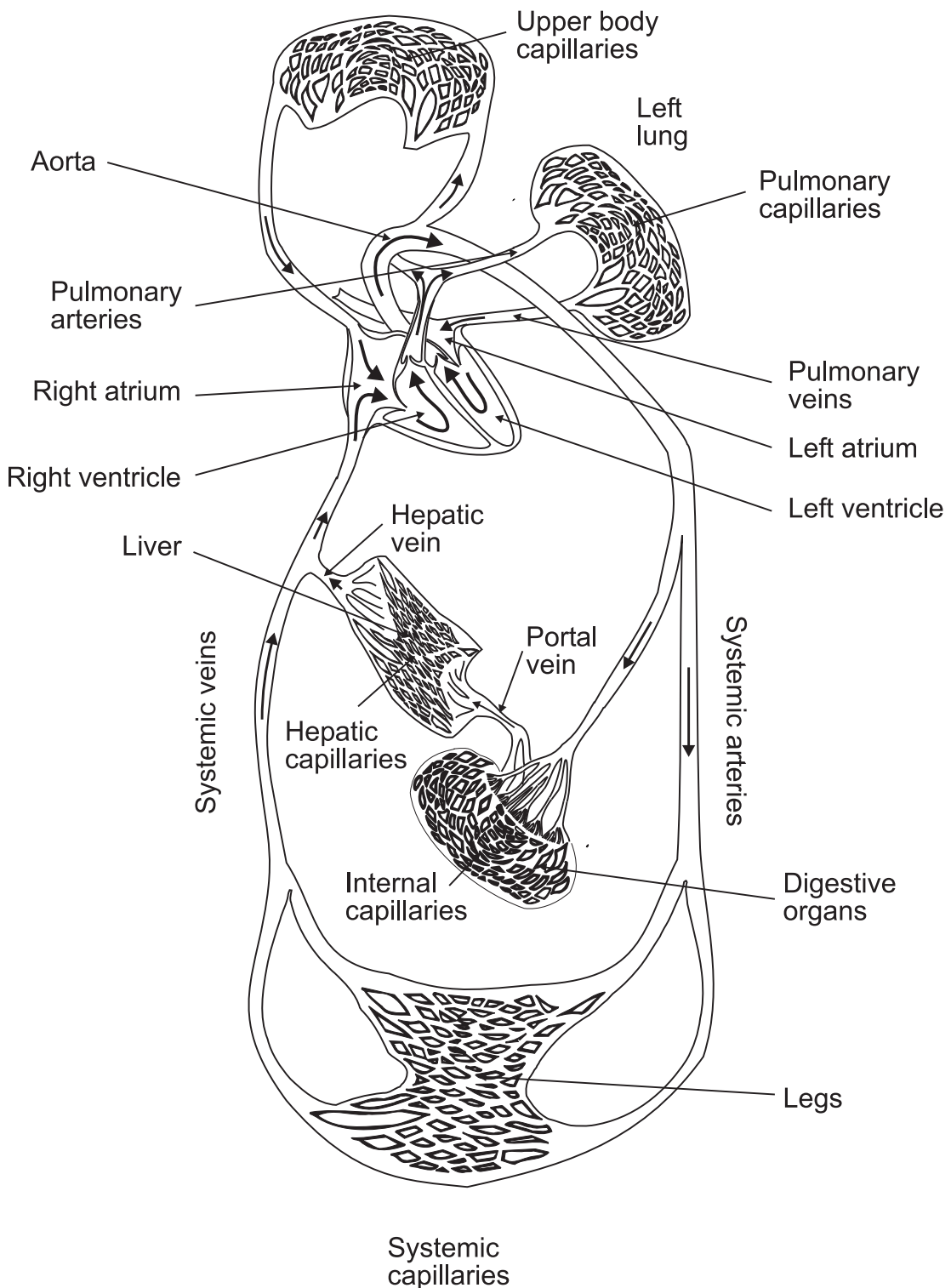


Figure 2.5: Circulatory system of the human body [32]

perform these vital functions. Initially, blood is discharged from the left ventricle of the heart through the aorta and travels to all areas of the body through multiple branches of the arterial tree. When blood flows through the arteries, it enters smaller channels known as arterioles. These arterioles lead to a network of tiny capillaries through which nutrients and waste materials are exchanged between the blood and the organs. The capillaries connect to form a network of venules, which supply the veins and deliver blood back to the heart. This system, in its entirety, is called systemic circulation. A diagram of the circulatory system as described above can be seen in fig. 2.5. In summary, when examining the elements that comprise the circulatory system, it consists of several components:

- Heart, the primary organ of the circulatory system that maintains blood pressure and controls blood velocity.
- Blood, and its sub-components
 - Plasma, which forms the primary volume, contains nutrients and formed cellular elements.
 - Red and white blood cells, which carry oxygen and fight off infections, respectively.
 - Platelets, which are also known as thrombocytes, have the function of clotting during blood vessel injury.
- Blood vessels
 - Arteries (and arterioles), transport oxygenated blood to organs and tissues at high pressure and velocity.
 - Capillaries are thin but wide-ranging blood vessels that perform the exchange of matter between the circulatory system and tissue.
 - Veins (and venules) carry blood back to the heart at low pressure and velocity.

2.2.1 Blood flow

Blood flow is the amount of blood that goes through a blood vessel in a particular period of time, and has a complicated flow pattern due to its pulsing flow. Advanced analysis of haemodynamics is not within the scope of this report, so the explanation will be brief. The primary forces that determine the blood flow F are the pressure difference across a blood vessel and vascular resistance. It is determined by Ohm's law as in eq. (2.16).

$$F = \frac{\Delta P}{R} \quad (2.16)$$

Where ΔP is the pressure difference across the blood vessel and R is the vascular resistance. The pressure difference ΔP is calculated with eq. (2.17).

$$\Delta P = P_1 - P_2 \quad (2.17)$$

Where P_1 and P_2 are the blood pressures measured at each end of the blood vessel. Pressure has a significant importance on blood flow because an increase in arterial pressure not only increases the force that pushes blood through the capillaries but also expands the vessels, lowering vascular resistance. Selected dimensions and flow characteristics can be seen in table 2.3.

Table 2.3: Typical dimensions and flow in human circulatory system [32]

Vessel	Internal diameter (cm)	Wall thickness (cm)	Length (cm)	Young's modulus (N/m ² ·10 ⁵)	Peak velocity (cms ⁻¹)	Mean velocity (cms ⁻¹)	Reynolds number (peak)	Pulse propagation velocity (cms ⁻¹)
Ascending aorta	1–2.4	0.05–0.08	5	3–6	20–290	10–40	4500	400–600
Descending aorta	0.8–1.8	0.05–0.08	20	3–6	25–250	10–40	3400	400–600
Abdominal aorta	0.5–1.2	0.04–0.06	15	9–11	50–60	8–20	1250	600–700
Femoral artery	0.2–0.8	0.02–0.06	10	9–12	100–120	10–15	1000	800–1030
Carotid artery	0.2–0.8	0.02–0.04	10–20	7–11				600–1100
Arteriole	0.001–0.008	0.002	0.1–0.2		0.5–1		0.09	
Capillary	0.0004–0.0008	0.0001	0.02–0.1		0.02–0.17		0.001	
Inferior vena cava	0.6–1.5	0.01–0.02	20–40	0.4–1	15–40		700	100–700

2.3 Transducer

Various transducer types are used during the testing of this project. Initially, commercially available transducers were used in order to validate the experimental process of the pulse-echo and Doppler measurements. Commercially available transducers in this context means *PZT* piezoelectric transducers. PZT is a piezoelectric material that deforms when an electrical voltage is applied, and generates an electrical signal when it is mechanically deformed. PZT transducers are widely used for medical imaging due to their high piezoelectric efficiency, high bandwidth and durability.

At a later stage during the project, CMUTs are used. CMUT, is a newer technology that uses capacitance to convert between electrical and mechanical energy. The transducer consists of a flexible membrane that moves in response to an applied voltage, producing ultrasound signals. CMUTs have advantages in terms of their small size, high frequency, and ability to operate in a broad range of conditions, making them ideal for use in portable and high-resolution imaging devices. They can be produced in large quantities using micro-machining processes that ensure tight parameter specifications, which is difficult to achieve with piezoelectric transducers. Fabricating CMUTs is also simpler than piezoelectric transducers, and batch processing allows for the creation of transducer arrays with various geometries and operating frequencies on a single wafer. The use of standard IC processes also makes it convenient to integrate CMUT arrays with supporting electronics. Additionally, CMUTs can operate over a wider temperature range than piezoelectric devices. Over the last decade, results have demonstrated that CMUTs optimized with regard to design parameters such as device size, membrane radius, thickness, shape, gap height, and operating mode can compare favourably to piezoelectric transducers in terms of bandwidth (170 %), frequency range (100 kHz to 70 000 kHz), dynamic range (130 dBV⁻¹), maximum output pressure (35 kPaV⁻¹), and receive sensitivity (50 dBPa⁻¹Hz⁻¹). There are two types of CMUTs used:

Rigid CMUTs:

- Advantages:
 - Higher mechanical stability, leading to less noise and improved image quality
 - Can handle higher pressures, making them suitable for deeper imaging applications
 - Can have a larger surface area, providing higher sensitivity
- Disadvantages:

Ret til med
enhed

- Less flexible, limiting their use in applications with complex geometries or limited access
- Higher stiffness, leading to increased power consumption and difficulty in producing high-frequency signals

Flexible CMUTs:

- Advantages:

- More flexible, allowing them to conform to complex geometries or be used in applications with limited access
- Can be made thinner and lighter, making them suitable for portable or handheld imaging devices
- Can be integrated into wearable devices or implanted into the body, enabling new imaging modalities

- Disadvantages:

- Lower mechanical stability, leading to increased noise and reduced image quality
- Lower maximum operating pressure, limiting their use in deep imaging applications
- Smaller surface area, resulting in reduced sensitivity

In summary, the choice between rigid and flexible CMUTs depends on the specific requirements of the application and the trade-off between flexibility, sensitivity, and image quality. For this project, a wearable transducer is desired and therefore the flexible CMUT is preferred.

Structure

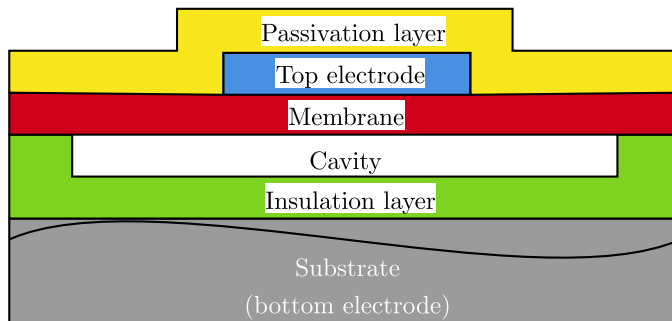


Figure 2.6: Basic CMUT structure

The key components of the structure are the cavity, membrane, and electrode. CMUT transducers are fabricated using standard integrated circuit (*IC*) fabrication processes, resulting in a capacitor cell that consists of a metallized membrane (top electrode) suspended above a heavily doped silicon substrate (bottom electrode), as depicted in fig. 2.6. An insulating layer is included to prevent the two electrodes from making contact and shorting. A single transducer element consists of multiple small capacitor cells connected in parallel. By arranging transducer elements in various geometries, any array shape can be achieved, as demonstrated in fig. 2.7. In (a), circular membranes with a diameter of 24 µm have approximately 50 % active area coverage. In (b), circular membranes with a diameter of 80 µm have 72 % active area coverage. (c) displays hexagonal membranes with a diameter of 80 µm that have 86 % active area coverage. Finally, (d) demonstrates tented membranes in which the etch holes are located on the post, providing over 90 % active area coverage.

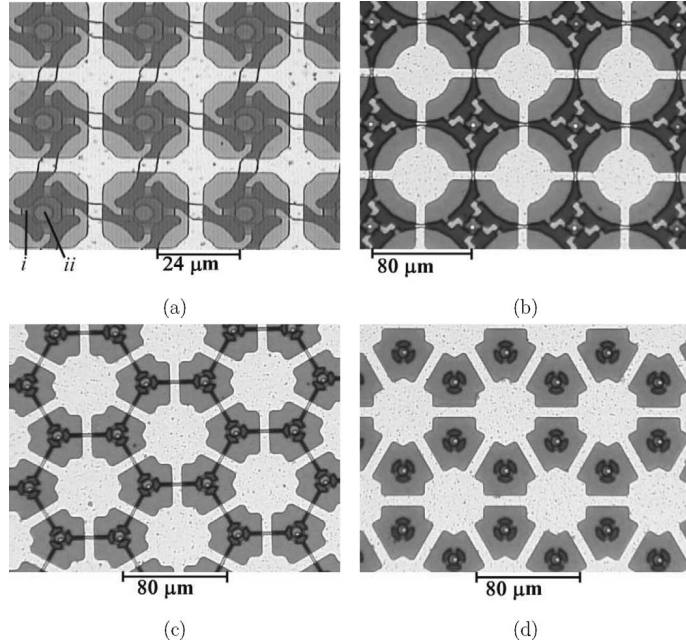


Figure 2.7: Optical images of various cMUT elements with different membrane shapes and sizes are shown to illustrate their relationship to active area coverage [17]

2.3.1 Impedance matching

Impedance matching refers to the adjustment of the output impedance of the transducer to match the input impedance of the receiving system, such as the ultrasound machine or amplifier. This ensures maximum transfer of energy from the transducer to the receiving system, leading to improved signal strength and reduced noise in the final image. In ultrasound imaging, the transducer is used to both transmit and receive ultrasound signals. The impedance of the transducer must be carefully matched to the environment it is operating in, to ensure efficient transfer of energy both ways. If the impedance of the transducer and the receiving system do not match, a portion of the transmitted energy will be reflected back to the transducer, leading to reduced signal strength and increased noise in the final image. This can also result in increased power consumption and reduced battery life in portable or handheld imaging devices.

2.4 Devices

A device that measures the flowing of blood is called a flowmeter. Flowmeters may be used both inside and outside of vessels. One of the flowmeters that may be used outside the vessel to monitor flow is *US*. Figure 2.8 depicts an ultrasonic wave of frequency f insonifying a blood artery, resulting in an angle of θ relative to velocity v . For simplicity, it is assumed that blood flows in a vessel at a constant velocity v . The echoes returned are shifted in frequency as described in eq. (2.15) earlier in the chapter. The echoes scattered by blood after being insonified by an ultrasonic wave convey information about the velocity of blood flow. Blood flow measurements are often used in clinical settings to determine the status of blood vessels and organ functioning. The two commonly used fundamental techniques for ultrasound Doppler flow measurements are continuous-wave (*CW*) and pulsed-wave (*PW*). Both will be explained.

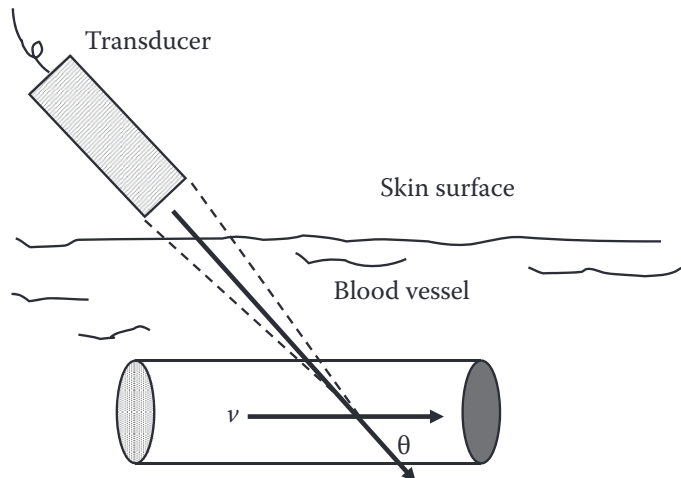


Figure 2.8: Diagram of *US* wave transmitted and reaching blood vessel with incident angle θ [39]

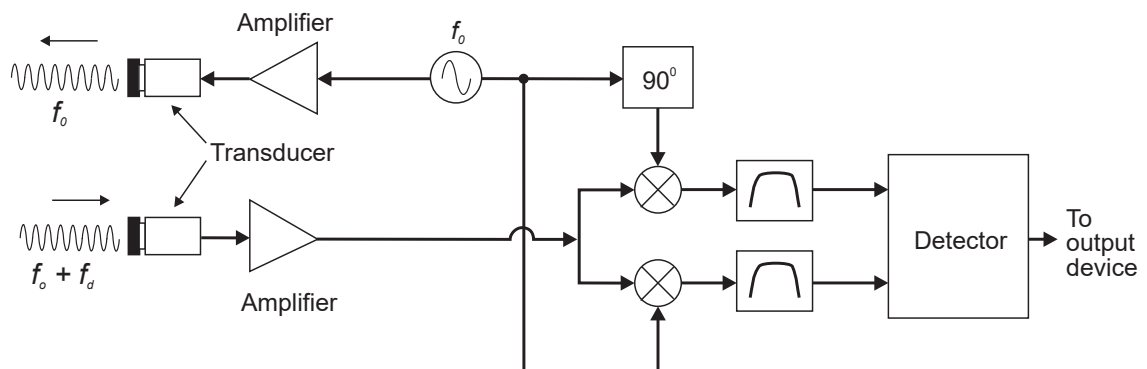


Figure 2.9: Block diagram of *CW* flowmeter [32]

2.4.1 Continuous-wave Flowmeter

The earliest non-invasive cardiovascular diagnostic technologies relied heavily on *CW* Doppler flowmeters. To continuously transmit waves and receive signals from moving reflectors, the *CW* flowmeter uses two transducers. *CW* flowmeters use less sophisticated electronics than *PW* flowmeters. A drawback to the *CW* flowmeter is the lacking depth discrimination due to the continuous characteristic of this device type. A block diagram of a typical *CW* flowmeter can be seen in fig. 2.9. The basic principles of the device are previously explained in section 2.1.4, and the measurement of the device is described in eq. (2.11). The device continuously emits an ultrasonic wave in the first transducer expressed as a function of time by eq. (2.18) [32].

$$e(t) = \cos(2\pi f_0 t) \quad (2.18)$$

While receiving the backscattered signal on the second transducer expressed by eq. (2.19) [32].

$$r_s(t) = a \cos(2\pi f_0 \alpha(t - t_0)) \quad (2.19)$$

$$\alpha \approx 1 - \frac{2v_z}{c} \quad (2.20)$$

$$\alpha t_0 \approx \frac{2d_0}{c} \quad (2.21)$$

Where v_z indicates the velocity in the z direction. Applying the Fourier transform, the expression yields eq. (2.22).

$$r_s(t) \cdot e^{j2\pi f_0 t} \iff R_s(f - f_0) \quad (2.22)$$

Where $R_s(f - f_0)$ is the Fourier transform of $r_s(t)$. The received signal is then multiplied with a quadrature signal of frequency f_0 to find the Doppler frequency in eq. (2.23).

$$m(t) = a [\cos(2\pi f_0 t) + j \sin(2\pi f_0 t)] \cos(2\pi f_0 \alpha(t - t_0)) \quad (2.23)$$

$$\begin{aligned} &= \frac{a}{2} \left\{ \cos(2\pi f_0 [(1 - \alpha)t - \alpha t_0]) + \cos(2\pi f_0 [(1 - \alpha)t - \alpha t_0]) \right. \\ &\quad \left. + j \sin(2\pi f_0 [(1 - \alpha)t - \alpha t_0]) + j \sin(2\pi f_0 [(1 - \alpha)t - \alpha t_0]) \right\} \end{aligned} \quad (2.24)$$

As is general for quadrature demodulation, the resulting signal contains the frequency components of the sum and difference of the emitted and received signals' frequencies shown in fig. 2.10, where the signals are shown in time and frequency domains.

Generally, a band-pass (*BP*) filter is used on the demodulated signal to remove the high-frequency summed signal at twice the frequency of f_0 . The filtered signal after the *BP* filter is expressed by eq. (2.25) and contains the Doppler shift of the emitted signal.

$$m_f(t) \approx \frac{a}{2} e^{(j2\pi f_0 \frac{2v_z}{c} t)} e^{(-j2\pi f_0 \alpha t_0)} \quad (2.25)$$

Where the second exponential term is the delay proportional to the time between transmission and receiving of the signal. The selected cutoff frequency is chosen to be much lower than the carrier frequency to remove the carrier wave. One issue with ultrasonic Doppler blood flow monitoring is that the blood vessels that generate large reflected echoes are also moving with a low velocity. These big, slow-moving echoes are referred to as clutter signals in Doppler nomenclature. The band pass filter's low-end cutoff frequency must be designed to minimize interference from these clutter signals. The design of this band pass

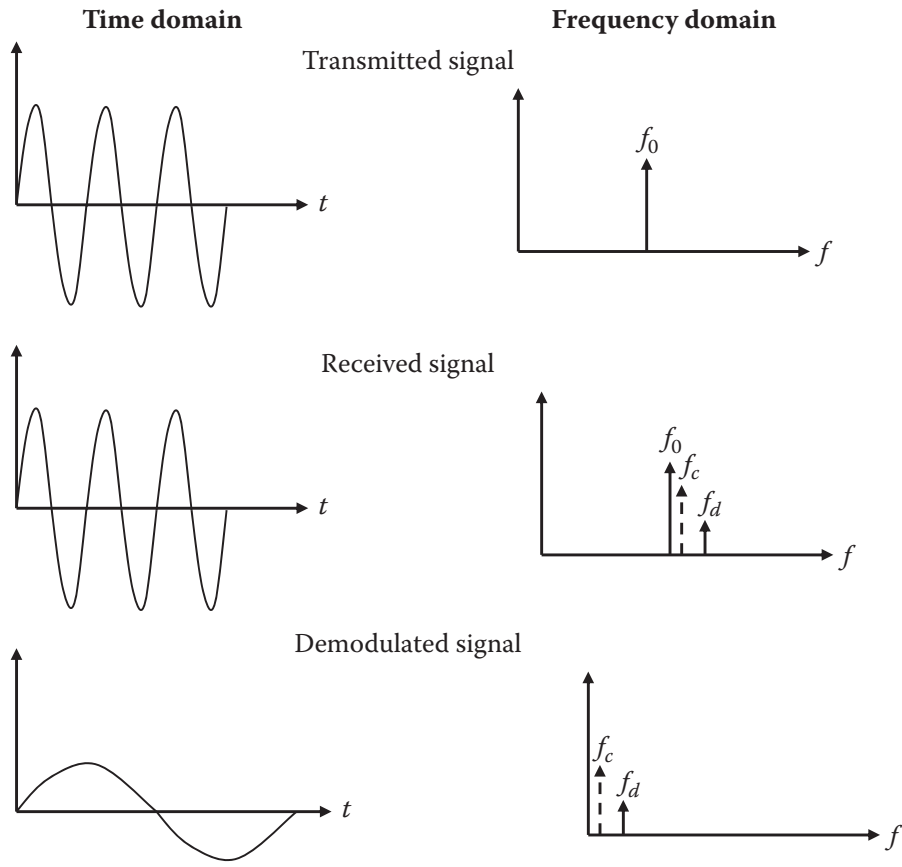


Figure 2.10: Demodulation effects of Doppler signals in time and frequency domain [39]

Table 2.4: Measured frequency shifts with a Doppler 3 MHz transducer at various velocities at a 45° incident angle [32]

Velocity (v) m/s	Doppler frequency (f_d) Hz
0.01	28
0.1	276
0.5	1377
1	2755
2	5510
5	13 770

filter in the low-frequency region, which serves the function of high pass, also known as a clutter rejection filter, has proven troublesome since the magnitude of clutter signals is many orders greater than that of blood and may obfuscate those from slow-moving blood.

Seen in table 2.4 is an example of measured Doppler frequencies using a 3 MHz transducer using the method shown in fig. 2.8. Note that the measured frequencies are all within the audible range.

2.4.2 Pulsed-wave Flowmeter

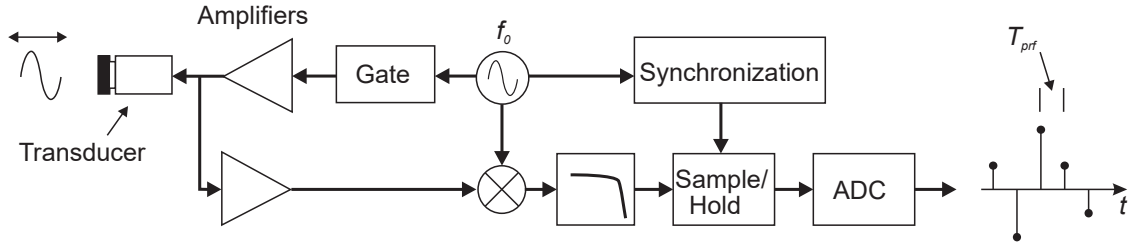


Figure 2.11: Block diagram of *PW* flowmeter [32]

The concept of a pulsed-wave flowmeter was proposed in [2] and other related articles. This type of flowmeter is periodically changing from a transmitter to a receiver. In the transmit mode, the transducer emits a series of pulses. When in the receiving mode, the transducer is listening for the backscattered signal. A simplified block diagram can be seen in fig. 2.11. The movement of particles within the blood causes a displacement in the backscattered signal. These systems are commonly referred to as “Doppler systems” even though it is somewhat misleading. The effects of attenuation are also causing a shift in frequency of a higher magnitude than the velocity of particles in the blood. This is because the conventional Doppler effect is not the straightforward methodology that is applied to the analysis of the back-scattered signal. It is, in fact, an artefact. It is the shift in the location of the scatters that is observed, not the shift in the transmitted frequency. Figure 2.12 shows the received signal after demodulation and filtering; the depth in tissue is fixed here, and the signals displayed on the left side of the figure are the result of a pulse sequence. Each line represents a single pulse, and each pulse is emitted at a pulse repetition frequency, f_{prf} . Instead, on the right, the dotted line shows the sampled signal formed by taking into account the amplitude of each pulse after a specified time period. To depict the signals on the graph, a single pulse is emitted for each line, and the signals are displaced in amplitude. The sampled signal is displayed on the right. In the pulsed-wave flowmeter, the received signal is described by eqs. (2.26a) to (2.26d) [32].

$$r_s(t) = a \cdot e^{(\alpha(t-t_0))} \quad (2.26a)$$

$$\alpha = \left(1 - \frac{2v_z}{c} \right) \quad (2.26b)$$

$$\alpha t_0 = \frac{2d_0}{c} \quad (2.26c)$$

$$v_z = |\vec{v}| \cos \theta \quad (2.26d)$$

Equation (2.27) provides the calculation for the time shift t_s of the RF signal between two emissions, which is determined by the distance that the scatterer moves in the direction of the ultrasound beam proportional to the velocity component v_z .

$$t_s = \frac{2v_z}{c} T_{\text{prf}} \quad (2.27)$$

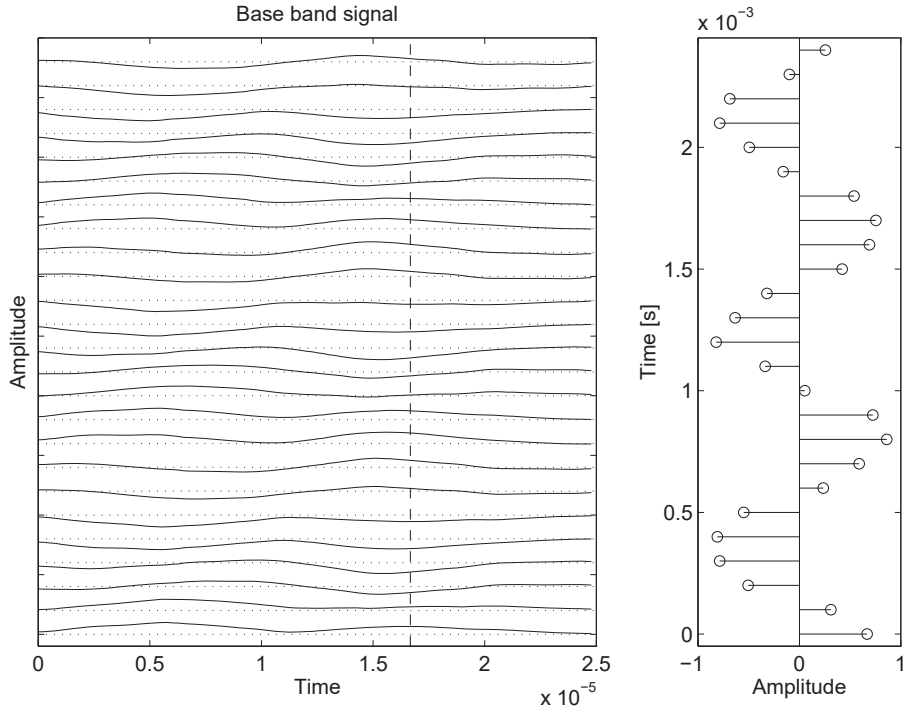


Figure 2.12: Sampling for a gate pulsed wave system with a single range [32]

Where c is the speed of sound in the medium, T_{prf} is the interval between each pulse emission. To measure the movement of the scatterer, the signal can be recorded at a certain depth. By selecting one sample at that specific depth for each line, a sampled signal with a frequency that corresponds to the scatter velocity can be obtained. Hypothetically, if the velocity of stationary scatterers in blood was measured, a constant amplitude would be measured. A change in the sample value is observed when there is movement. Between two pulses, the scatterer movement is proportional to the velocity v_z in the direction of the ultrasound beam. Taking one sample from each line at a certain depth yields a sampled signal with a frequency proportional to the scatter velocity. After the back-scattered signal is received it is multiplied by the center frequency of the emitted pulse and filtered to remove the sum frequency [32]. A analogue-to-digital converter (*ADC*) quantifies the signal for further signal processing. Referring to displacement fig. 2.12 again, the dashed vertical line represents the sample of each pulse that is taken. If sampling is done T_s after pulse emission, the measurement depth is expressed by eq. (2.28).

$$d_0 = \frac{T_s c}{2} \quad (2.28)$$

Thus, if a sample is taken at the same depth for each line, resulting in a sinusoidal signal proportional in frequency to the scatter velocity [15]. This technique improved the accuracy of the investigations of blood vessels and facilitated the display of velocity profiles. Equation (2.29a) describes the relationship between the received sampled signal for a single scatter and the sinusoidal pulse emitted by the transducer during the i^{th} pulse emission.

$$r(i) = a(i) \sin(2\pi f_p i T_{\text{prf}} + \theta) \quad (2.29a)$$

$$f_p = \frac{2v_z}{c} f_0 \quad (2.29b)$$

Where f_p is expressed by eq. (2.29b), $a(i)$ is the amplitude for the i^{th} pulse, f_0 is the emitted frequency, and θ is the phase factor proportional to the depth of interest.

2.5 Blood Velocity Estimation

This section will explain the methodology of velocity estimation, assuming a pulsed-wave system signal is obtained from a back-scattered signal. There are variations of methods that can be applied, but only the implementation that will be used is discussed in this report.

Separate CW
estimation

2.5.1 Spectral Envelope

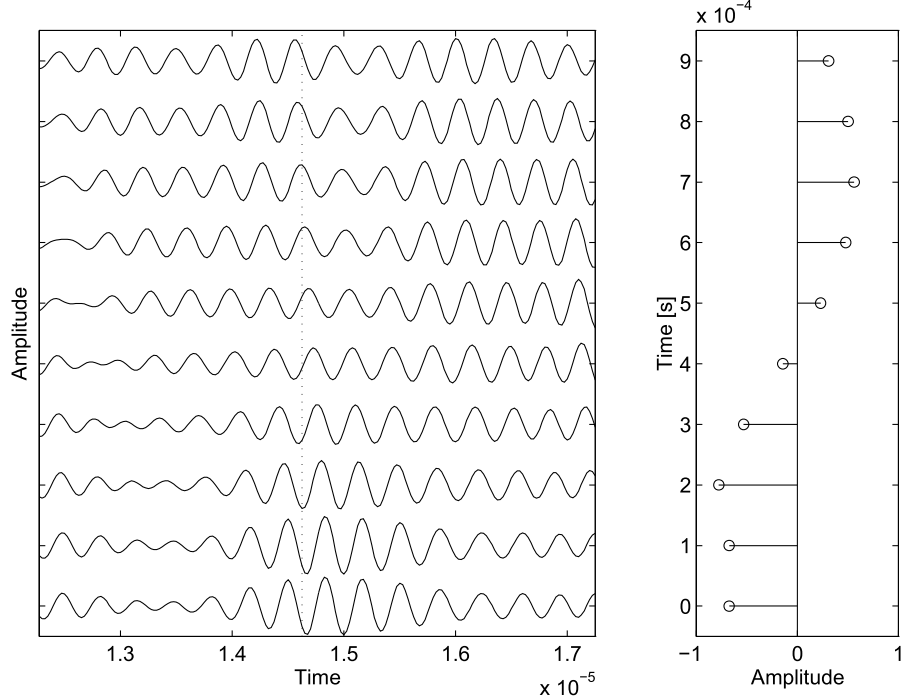


Figure 2.13: Simulated RF sampling of blood vessel with segmented receiver line with a sample interval denoted by a dotted line (left) and the resulting amplitude of the sample (right) [32]

Figure 2.13 displays a signal where the scatterers in the sampled depth d_0 move away from the transducer, the shift in the pulsed signal is present. The measurement is created by taking one sample at a specific depth (d_0) for each RF line. The sampling is performed at a frequency of f_{prf} , as indicated by the dotted line in the figure. Due to the slow movement of the received signals past the sample volume, there is a gradual change in the sampled signal over time. As a result of the slow movement of the signals, the frequency of the sampled signal is much lower than that of the RF signal. It's worth noting that the received signal not only shifts in time from pulse to pulse, but its shape also changes. This is because the signal is constructed by adding up responses from many scatterers that move at different speeds. A stationary structure will result in an identical sample value for all segmented RF lines. The spectrum of this stationary signal is shown in eq. (2.30).

$$|H_s(f)| = \left| a \frac{\sin(\pi f N T_{\text{prf}})}{\sin(\pi f T_{\text{prf}})} \right| \quad (2.30)$$

which for $f = 0$ is equal to aN and has its first zero at f_{prf}/N . The signal spectrum based on eq. (2.30) is shown in fig. 2.14.

When dealing with small blood vessels, the stationary echoes can be significantly stronger (up to 40 dB) than the blood signal itself. To properly visualize blood flow details, the

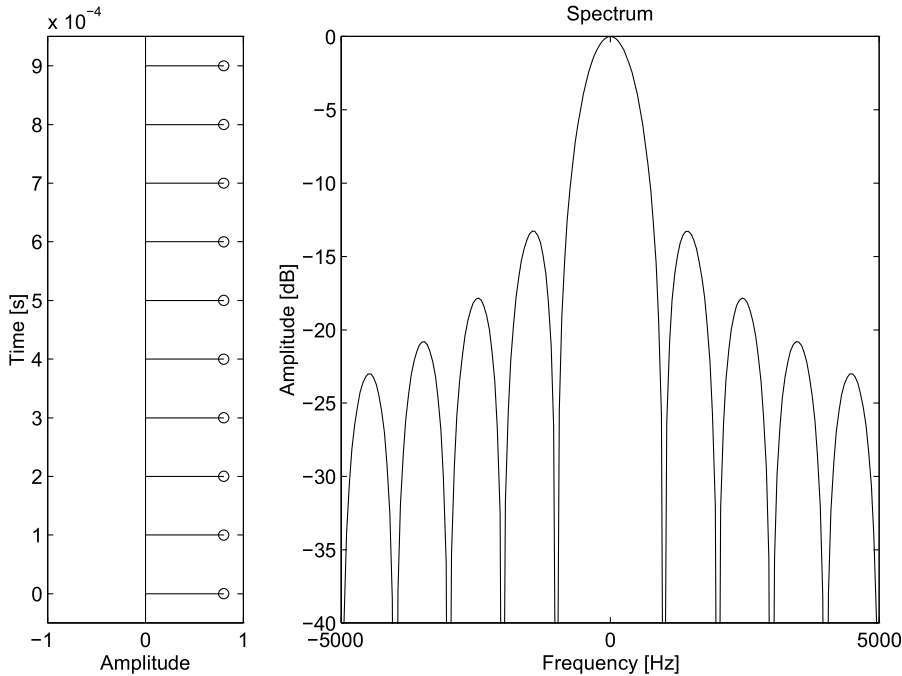


Figure 2.14: Stationary tissue sampled signal (left) and stationary tissue sample spectrum (right) [32]

stationary signal must be eliminated from the sonogram. This requires setting the cutoff frequency to at least $f_{\text{prf}} = N$, in order to remove the main component. In some cases, a higher cutoff frequency may be necessary, particularly if the stationary echo is strong or the vessel wall is in motion. The speed and pulse repetition frequency of a single moving scatterer affect the signal received. The signal will look like the pulse, but its time scale and frequency will differ from the RF pulse because the pulse waveform slowly moves past the point where it is measured. Figure 2.15 shows this, where a beam from a concave transducer is crossed by a single scatterer. The time shift between each line is determined by the expression in eq. (2.31).

$$t_s = \frac{2v_z}{c} \cdot T_{\text{prf}} \quad (2.31)$$

Which increases linearly by line i . Individual sinusoidal components are expressed by eq. (2.32).

$$y(i) = \sin \left(2\pi \frac{2v_z}{c} \cdot f_0 i T_{\text{prf}} \right) \quad (2.32)$$

Where the variable iT_{prf} corresponds to time and f_0 corresponds to the fundamental frequency. The received signal frequency is expressed by $\frac{2v_z}{c} \cdot f_0$, where the frequency axis is scaled by factor $\frac{2v_z}{c}$ as seen in fig. 2.16. The center frequency transforms to $f_p = \frac{2v_z}{c} f_0$. Every other spectral element is transformed by factor $\frac{2v_z}{c}$ and the received signal has the shape of a scaled frequency pulse. A sufficient number of lines must be captured, or only a part of the pulse is obtained. In practical terms, it corresponds to weighing the pulse with a rectangular window, which broadens the spectrum. The spectrum of the window is expressed by eq. (2.33) and is convolved with the spectrum of the pulse. A narrow spectrum is seen for slow velocities and the resulting spectrum is nearly determined solely by the spectrum of the window.

$$W(f) = \frac{\sin(\pi f N T_{\text{prf}})}{\sin(\pi f T_{\text{prf}})} e^{(-j\pi f N T_{\text{prf}})} \quad (2.33)$$

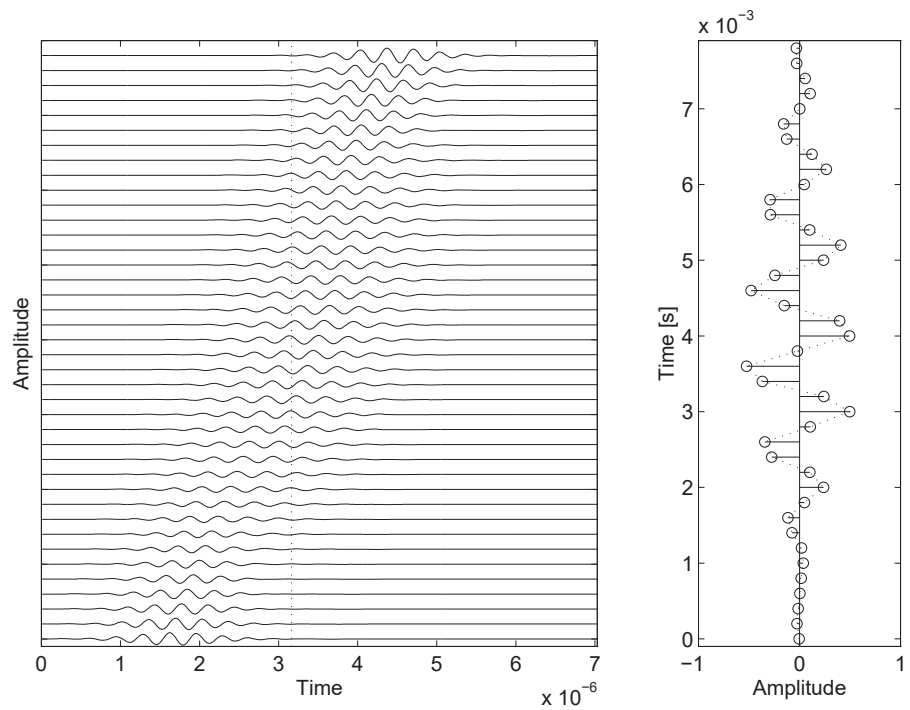


Figure 2.15: Single moving scatterer crossing a concave transducer beam [32]

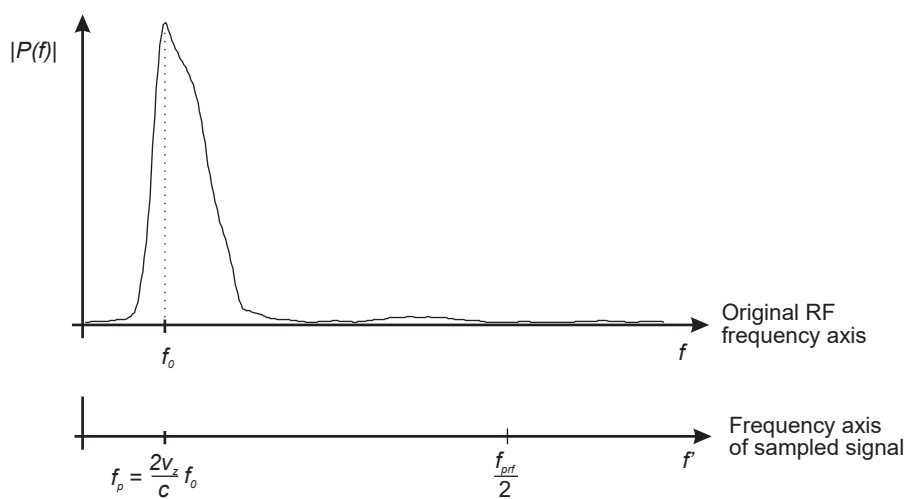


Figure 2.16: Frequency axis scaling for scatterer with velocity v_z [32]

This window limitation does not apply, as long as the whole pulse is sampled. If $NT_{\text{prf}} = cM/2v_z f_0$, the number of lines acquired and the width of the rectangular pulse are matched. A limitation on the lowest possible velocity and frequency is found through eqs. (2.34a) to (2.34c).

$$NT_{\text{prf}} = \frac{1}{\frac{2v_{\min}}{c} f_0} \quad (2.34a)$$

$$v_{\min} = \frac{c}{2} \cdot \frac{f_{\text{prf}}}{N f_0} \quad (2.34b)$$

$$f_{\min} = \frac{f_{\text{prf}}}{N} \quad (2.34c)$$

And conversely, the maximum velocity is determined by the pulse repetition frequency f_{prf} , as aliasing occurs at frequencies $f_{\text{prf}}/2$ or above. The relation of maximum velocity is expressed by eqs. (2.35a) and (2.35b).

$$\frac{f_{\text{prf}}}{2} \leq \frac{2v_{\max}}{c} f_0 \quad (2.35a)$$

$$v_{\max} = \frac{c}{2} \cdot \frac{f_{\text{prf}}}{2 f_0} \quad (2.35b)$$

However, this does not consider pulse bandwidth into account. In practice, the maximum velocity v_{\max} will be slightly lower.

2.5.2 One-Dimensional Velocity Estimation

If a pulsed sinusoidal signal, i.e. $p(t) = \cos(2\pi f_0 t)$, is emitted into an ultrasound field a number of times, the returned signal is sampled at a depth of interest, d_0 . The sampled signal of a monochromatic wave yields eq. (2.36).

$$r(k, l) = \cos \left(2\pi \left(\frac{f_0}{f_s} k - \frac{2v_z}{c} f_0 l T_{\text{prf}} \right) \right) \quad (2.36)$$

Where c is the speed of sound, v_z is the blood velocity component along the axial beam, f_0 is the carrier frequency, l is the emission times, k is the sample depth, T_{prf} is the time between each pulse burst, f_s is the sampling frequency, and $\varphi = 2\pi f_0 / f_s$ is the phase factor for the depth of interest. The returned signal frequency is given by eq. (2.37) and is proportional to the axial blood velocity component.

$$\psi = -2\pi \frac{2v_z f_0}{f_{\text{prfc}}} \quad (2.37)$$

To obtain positive and negative velocities, a one-sided spectrum should be used in the signal, which can be found with a Hilbert transform of the signal [33]. The sampled signal is expressed by eqs. (2.38a) and (2.38b).

$$r_q(k, l) = e^{j(\Phi k + \phi l)} \quad (2.38a)$$

$$\Phi = 2\pi \frac{f_0}{f_s} \quad (2.38b)$$

2.5.3 Sonography

Given that the frequency volume of the received signal is similar to the blood's velocity distribution, the Fourier transform of the received signal can be used to obtain velocity. The spectrogram, usually erroneously known as the Doppler spectrum, can be created by

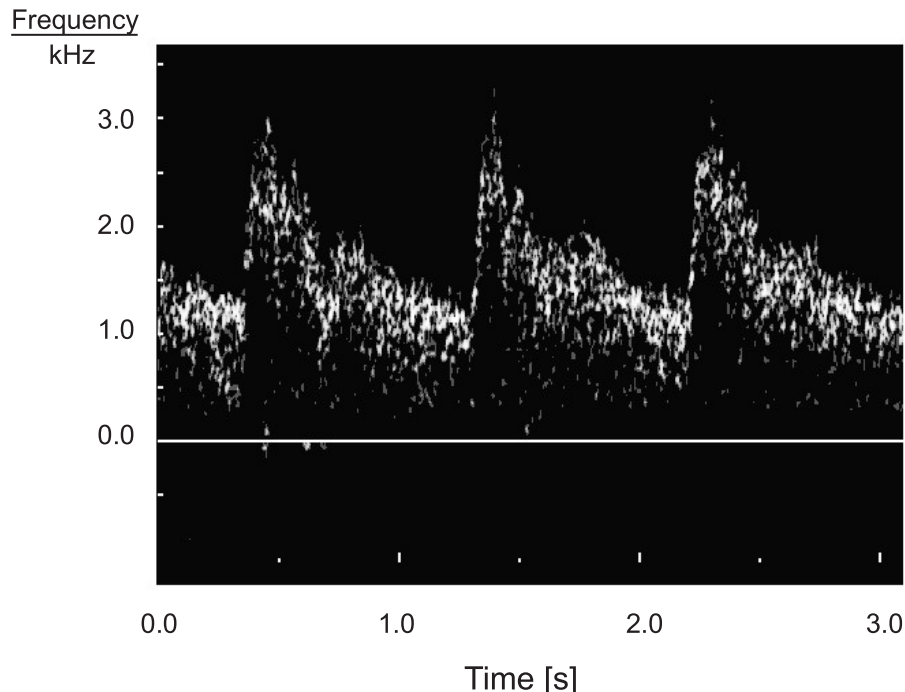


Figure 2.17: Arterial sonogram with time-frequency and Doppler shift [32]

saving the *PSD* together. The *PSD* is calculated for each of the components that make up the received signal in order to accomplish this. A quadrature demodulated signal is used to display both positive and negative frequencies. When these spectra are shown side by side, the evolution of the velocity distribution can then be seen. A sonography of an artery is displayed in fig. 2.17.

3 Synthesis

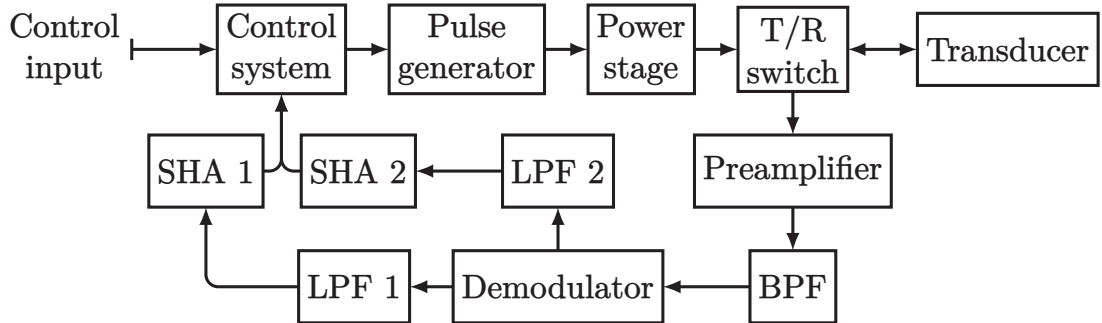


Figure 3.1: Simplified overview of the entire system

A simplified overview of the entire system can be seen in fig. 3.1. Each of the various modules will be explained during this chapter of the report. Initially, the control system will be briefly explained and the reasons for its design choice. Secondly, the signal chain in the transmitter will be outlined and how the transducer is driven by the power stage with the added protective switching circuit. Finally, the analogue front-end will be further explained with its various subcircuits for filtering, amplifying, demodulating, and sampling the signal. Lastly, the design of the digital signal processor (*DSP*) within the control system will be explained.

3.1 Control System

The choice of platform for the control system is a microcontroller. A microcontroller is a small computer that is built into a single *IC* chip. It includes a central processing unit (*CPU*), memory, and input/output (*I/O*) peripherals, and it is designed to perform a specific set of tasks. Microcontrollers are used in a wide range of electronic devices, including appliances, automobiles, industrial control systems, and consumer electronics. Microcontrollers are often used in applications where a small, low-power device is needed to perform simple tasks, such as controlling a motor or reading a sensor. They are usually programmed in a high-level language, such as C or C++, and they can be programmed to perform a variety of tasks, depending on the specific application. The chosen microcontroller unit (*MCU*) for this project is STM32F411RE, because it is sufficient for the application and sourcing limitations within the *IC* supply chain. For implementing the control system, a real-time operating system (*RTOS*) can offer multiple benefits for the embedded system development. A *RTOS* is an operating system that is designed to handle real-time applications. Real-time applications are those that require timely processing of data in order to function correctly. This can include tasks such as controlling industrial machinery, monitoring and controlling processes. Real-time operating systems are designed to prioritize certain tasks and ensure that they are completed within a specific timeframe. They do this by allocating a certain amount of processing resources to each task, and by interrupting the execution of lower-priority tasks as needed to ensure that high-priority tasks are completed on time. *RTOSs* typically include features such as preemptive scheduling, real-time communication, and support for multiple processors and hardware architectures. Alternatively, a vendor-locked baremetal implementation is an option, in this case STM32 HAL. Notable differences between the two approaches are, but not limited to:

- Multitasking: RTOS allows for parallel execution that enable more complex applications.
- Portability: Standard modules mean that the same code can be easily ported to other devices and even other platforms without modifications.
- Reduced development time: Especially for rapid prototype development, using pre-existing APIs significantly reduces development time by providing many of the low-level tasks such as scheduling, resource management, and timing by the operating system.

3.1.1 Development Environment

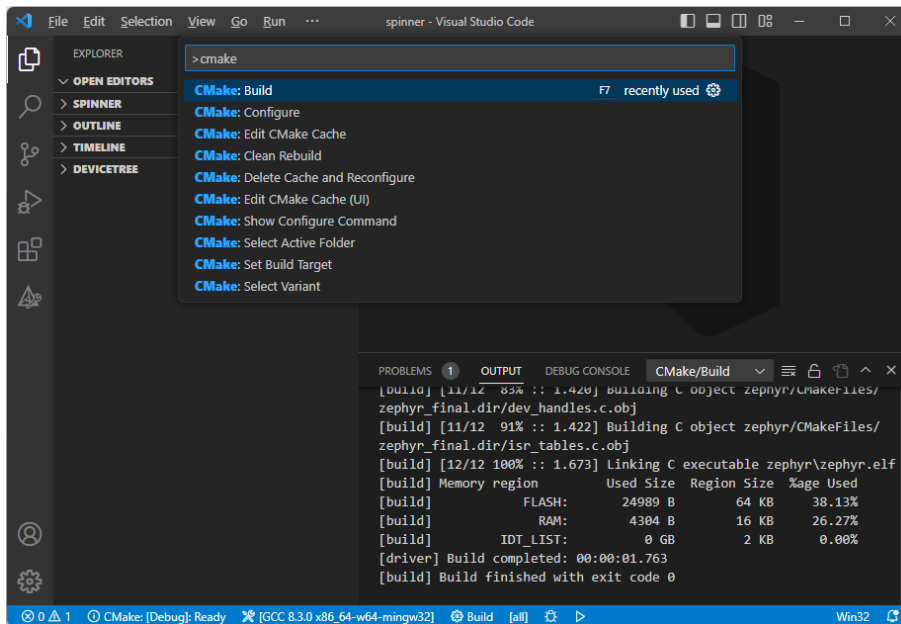


Figure 3.2: VSCode editor with CMake Tools active, displaying available tasks

Visual Studio Code (VSCode) is an open-source code editor developed by Microsoft. It is designed to be highly customizable and efficient, with a wide range of features and extensions that allow developers to customize their workflows and improve their productivity. VSCode works in synergy with CMake through an extension. CMake is a cross-platform build system that helps developers manage the build process for their projects. It is used to generate build files for different platforms and build systems, to build projects on a wide range of platforms. When using CMake with VSCode, the basic idea is to use the CMake extension for VSCode to generate the appropriate build files for the target platform, and then use the VSCode tasks and debugging capabilities to build and debug the project. After setup of VSCode, the CMake Tools [60] extension can be found in the VSCode Marketplace. The CMake Tools extension allows you to create, configure and build CMake projects from within VSCode. Once the extension is installed, you can create a new CMake project and configure it by specifying the path to the `CMakeLists.txt` file and other settings like the target platform and build configuration. After configuring the project, the VSCode tasks are provided to build and run the project. These tasks are defined in the `tasks.json` file, which can be customized to specify the build command and other options. Examples of tasks are build the project, cleaning the build directory, or running tests. The available CMake tasks are shown in fig. 3.2. In addition to building and running the project, VSCode allows for debugging capabilities to debug code.

3.1.2 Zephyr

Zephyr is an open-source *RTOS* designed to be lightweight and run on a wide range of devices, from *MCUs* with as little as 20 kB of random access memory (*RAM*) to more powerful systems with multiple processors. Zephyr is designed to be modular and scalable, with a focus on security and low power consumption. It includes support for a wide range of hardware architectures, including ARM Cortex-M, x86, and RISC-V, and it can be used with a variety of development boards and microcontrollers. One of the key features of Zephyr is its ability to run on very small devices with limited resources. It includes support for various networking protocols, such as bluetooth low energy (*BLE*), IPv4, and IPv6, which makes it well-suited for use in Internet of Things (*IoT*) applications. Zephyr is developed as part of the Linux Foundation's Zephyr Project, and it is widely used in the development of IoT and embedded systems.

Build System

To build an application with the Zephyr kernel, you use CMake which has two phases - configuration and build. During configuration phase, CMake executes the `CMakeLists.txt` build scripts to generate an internal model of the Zephyr build. Starting with device tree source (*DTS*) and device tree source include (*DTSI*) and then using the device-tree nodes and Kconfig to configure the set of build files for ninja. Seen in fig. 3.3 is the

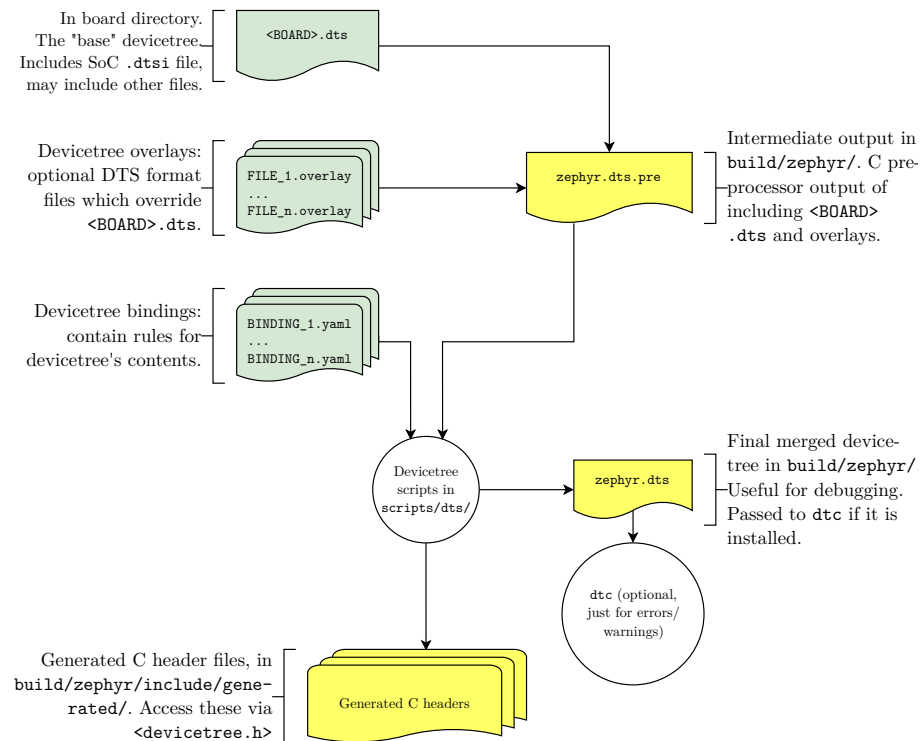


Figure 3.3: Devicetree input files (green) and output files (yellow) [58]

process in which the build system searches out device-trees in certain locations and merges them into the `zephyr.dts` that will be used for configuring and mapping every peripheral. Typically, each supported board has a file called `BOARD.dts` that defines the hardware of the board. The `BOARD.dts` file includes one or more `.dtsi` files that describe the CPU or system-on-chip that Zephyr runs on, and other common hardware features shared by multiple boards. These `.dtsi` files may also include other `.dtsi` files. Additionally, the `BOARD.dts` file provides a description of the specific hardware of the board. After parsing the `BOARD.dts` file, the main point being the merge with the `.overlay` file specific to both the project and the board. This overlay enables the portability feature of Zephyr. A

significant degree of the workload when implementing Zephyr projects are thus in writing hardware devicetrees and then writing as generic firmware implementations as possible. Next, the configuration phase can be seen in fig. 3.4. Once configuration phase is done, CMake generates build scripts that are native to the host platform and initiate the build sequence with the build system Ninja [56]. Afterwards, the generated build scripts are executed to begin the second phase, build. The build scripts can recompile the application without involving CMake after most code changes. Zephyr uses the “target” concept of CMake to organize the build, where a target can be an executable, a library, or a generated file. The final output of Ninja is a binary file ready for flashing using a microcontroller programmer.

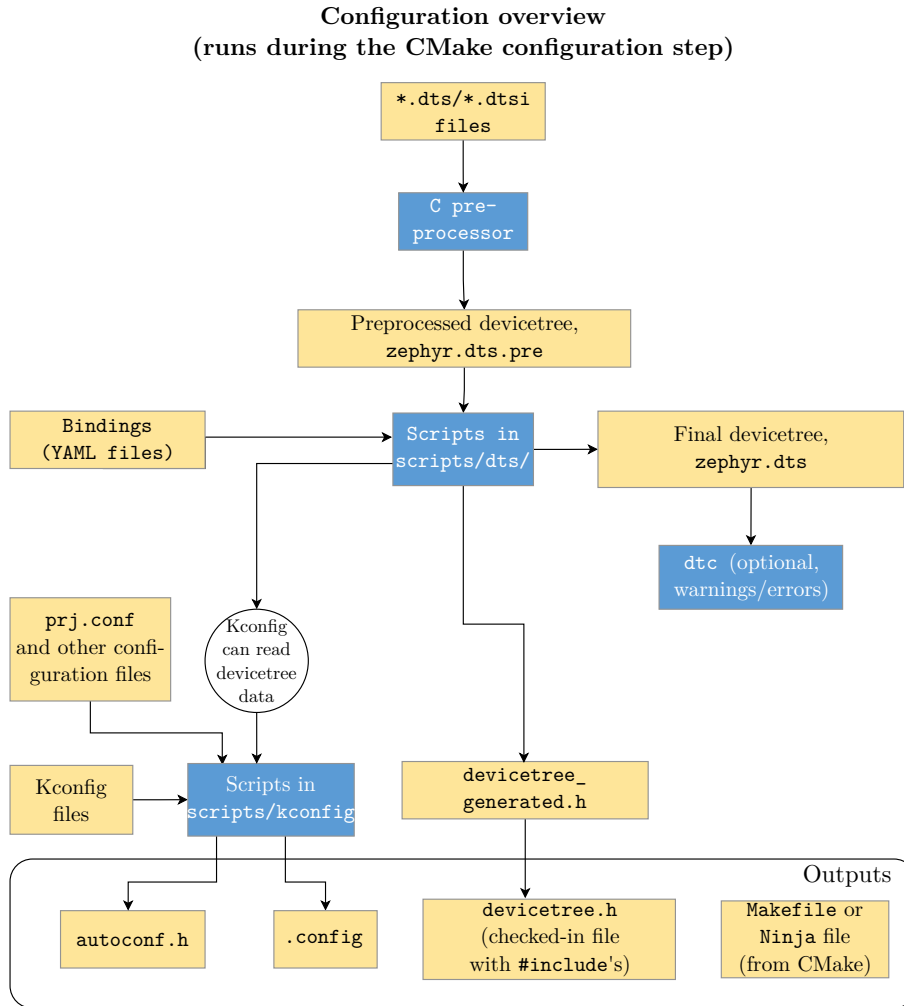


Figure 3.4: Configuration phase of a Zephyr application [58]

After cmake configuration phase has completed, the build phase begins. CMake invokes the build system, which (conceptually) has five (six, one is repeated) stages: (I) pre-build, (II) generation and compilation, (III) first-pass binary (and (IV) second-pass binary), (V) final binary and (VI) post-processing. In fig. 3.5 the build system binds system call functions to implementations. Next, in fig. 3.6 the build system collects source files for various subsystems (decided by the configuration phase) and compiles into archives. The `gen_app_partitions.py` script examines all the archives that are produced and creates linker scripts that organize and align application partitions correctly, based on the memory protection hardware of the target. Then `cpp` process involves merging linker script fragments from

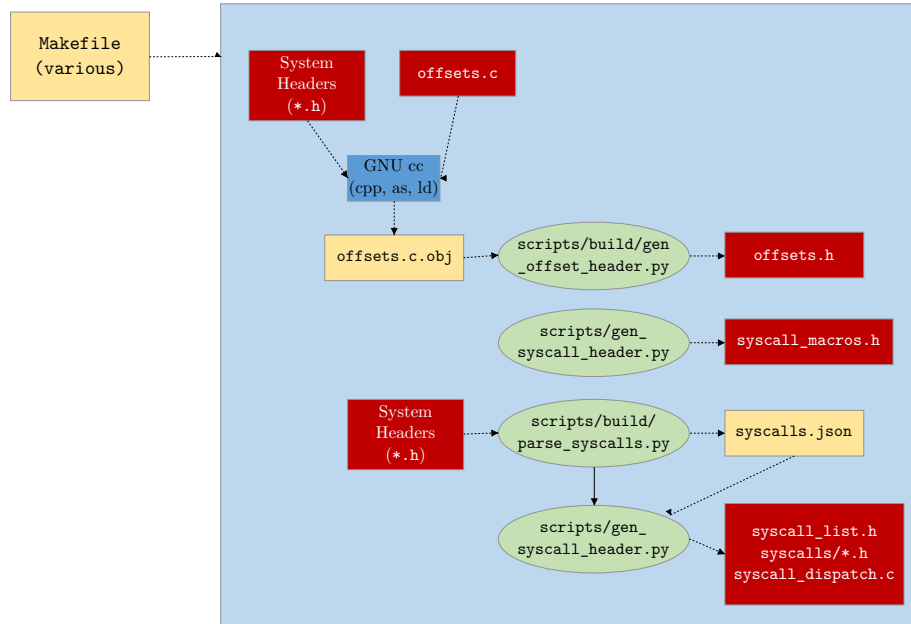


Figure 3.5: Flowchart of build stage I, pre-build

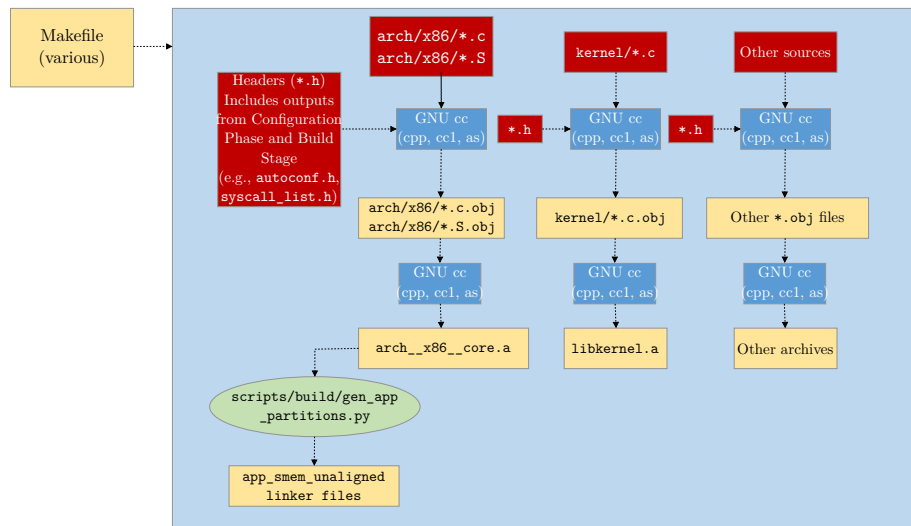


Figure 3.6: Flowchart of build stage II, generation and compilation

various sources, including the target's architecture/system-on-a-chip (*SoC*), the kernel tree, partition output (if memory protection is enabled), and any other selected fragments from the configuration process. These are combined into a `linker.cmd` file. The compiled archives are then linked with `ld`, following the specifications in the `linker.cmd` file. Shown

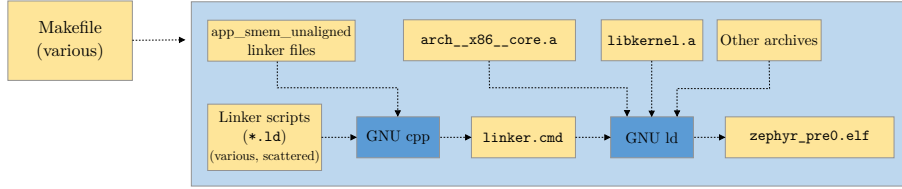


Figure 3.7: Flowchart of build stage III, intermediate binary

in fig. 3.7 is the process, in which an unfixed size intermediate binary is produced. If a devicetree is being used, an intermediate binary is generated that has a variable size. The binary is not fixed in size, which means that it can be modified by post-processing steps that affect the size of the final binary. In Figure 3.8 the fixed size intermediate binary is

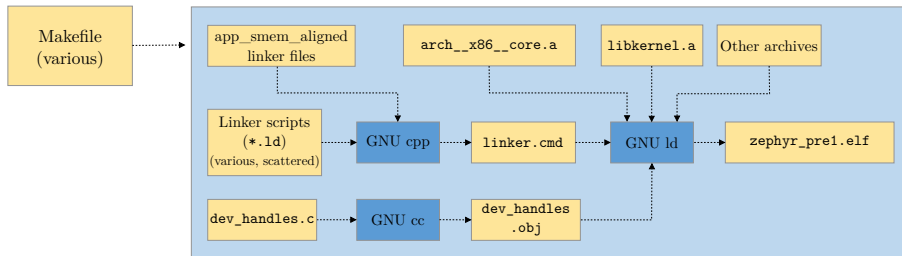


Figure 3.8: Flowchart of build stage IV, second intermediate binary

generated. The previous stage's binaries are not fully formed and contain sections that are empty or marked as placeholders. These sections must be filled in by a process similar to reflection. To finish building, certain scripts are run on the intermediate binaries. These scripts generate the necessary components that are missing from the final binary. Next, in

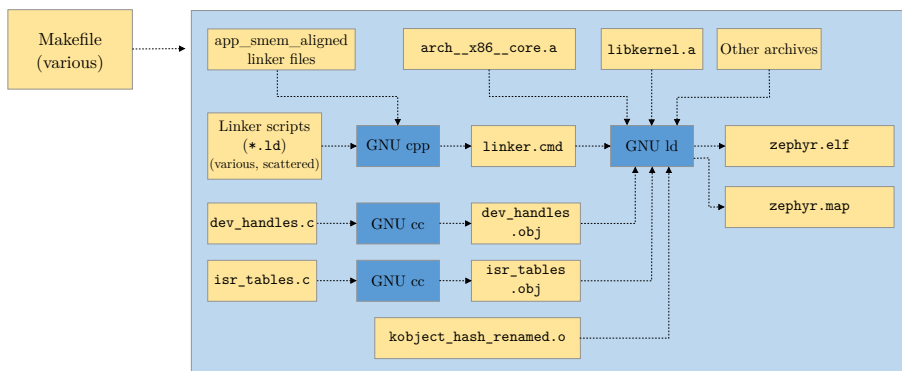


Figure 3.9: Flowchart of build stage V, final binary

fig. 3.9, the final binary is produced by repeating the link from the previous stage, but this time with all the missing pieces populated. Finally, in fig. 3.10, using `GNU objdump`, the completed kernel is converted from a executable and linkable format (*ELF*) file to the hex file that is expected by the flash tool compatible with the target device.

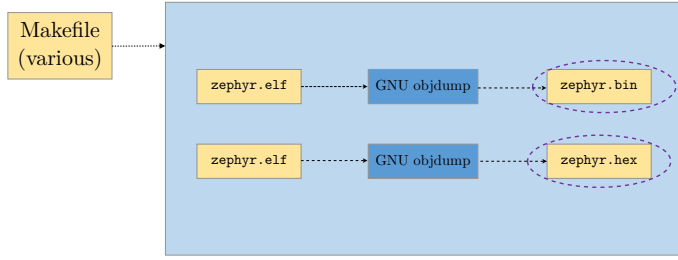


Figure 3.10: Flowchart of build stage VI, post-processing

3.2 Pulse Generator

Initially, a pulse generator was designed by using a programmable synthesizer circuit, but due to constraints within generating complementary PWM with dead-time when driving the half-bridge, a timer based PWM generation in the *MCU* is preferable. In a half-bridge power stage, dead-time refers to the amount of time that elapses between the moment when one of the switches in the half-bridge (either the high-side or the low-side switch) turns off and the moment when the other switch turns on. During the dead-time, both switches in the half-bridge are off, which means that there is no current flowing through either switch in the half-bridge. A scenario where both switches are on, can cause problems if the output of the half-bridge is connected to a load, as it may cause the load to behave erratically or even be damaged. To avoid these problems, it is important to carefully consider the amount of dead-time in a half-bridge power stage. In general, a longer dead-time will reduce the risk of damage to the load, but it will also reduce the efficiency of the power stage, as energy will be lost during the dead-time. Therefore, it is important to carefully balance the trade-off between efficiency and safety in order to determine the optimal amount of dead-time for a given half-bridge power stage. Based on discussions during design review, it was decided to change approach and generate the two complementary PWM signals by configuring the PWM module of the microcontroller with the functionality though with a trade-off in resolution. However, for this application there is no need to amplitude modulate the output signal and therefore no downside. In the context of a PW Doppler system, it is desired to generate 3 PWM signals:

- 5 MHz complementary signal with dead-time for the pulsed burst during transmit mode.
- 10 kHz signal as f_{prf} for the timing control of the transmit/receive switch.
- 20 MHz clock signal for the demodulation circuit in the receiver.
- 10 kHz gate pulse for S/H control with pulse length $t_{\text{pulse}} = N_{\text{pulse}} \times T_{\text{prd}}$, where $T_{\text{prd}} = 1/f_{\text{pwm}}$

3.3 Power Stage

Several MOSFET drivers were considered, e.g. ISL55111[53], EL7104[20], and MD1213[45]. The MD1213 has an advantage over the ISL55111 or EL7104 for ultrasound MOSFET drivers since it is specifically designed for high-voltage P-channel and N-channel MOSFETs in medical ultrasound and other applications needing a high output current for a capacitive load. It has a high-speed input stage with a logic interface that can function from 1.8 V to 5 V and an ideal operating input signal range of 1.8 V to 3.3 V. The DC-coupled adaptive threshold circuit sets the level translator switch threshold to the average of the input

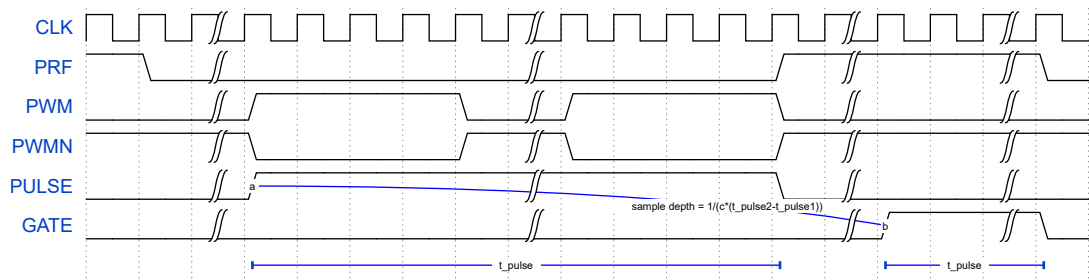


Figure 3.11: Timing diagram of various control signals for an arbitrary n length pulse chain expressed by the second diagram gap

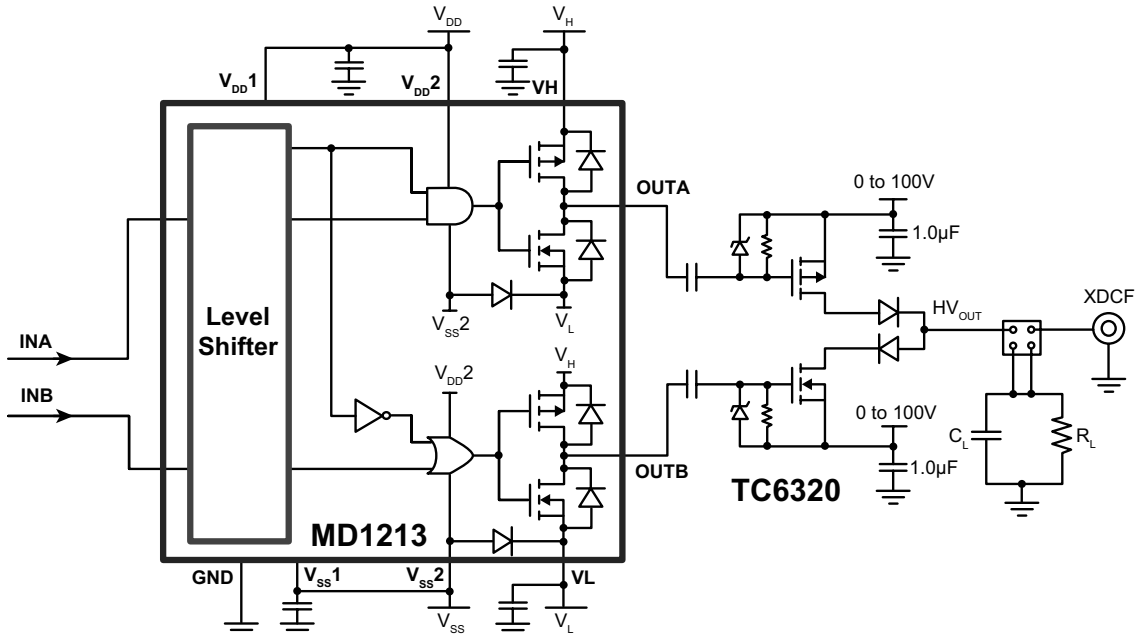


Figure 3.12: Block diagram of power stage [36]

logic LOW and logic HIGH levels. Consequentially, the MD1213 is designed primarily for driving MOSFETs in medical ultrasound applications, whereas the ISL55111 and EL7104 are more general-purpose drivers that may not perform as well in ultrasound applications. The MD1213's output stage has a distinguishing features in that the LOW and HIGH levels of the output signal may be set independently of the rest of the circuit's supply voltages. The input logic levels, for example, might be 0 V and 1.8 V, whereas the control logic is powered by +5 V to -5 V. The output LOW and HIGH values, on the other hand, may be changed between -5 V to +5 V. This gives you greater flexibility in adjusting the output signal levels to meet individual needs. The output stage may also provide peak currents of up to 2 A, depending on the load capacitance and supply voltages employed. Seen in section 3.3 is the circuit diagram of the power stage with the gate driver on the left side and the half-bridge on the right side. Using a SPICE macro model, an LTspice

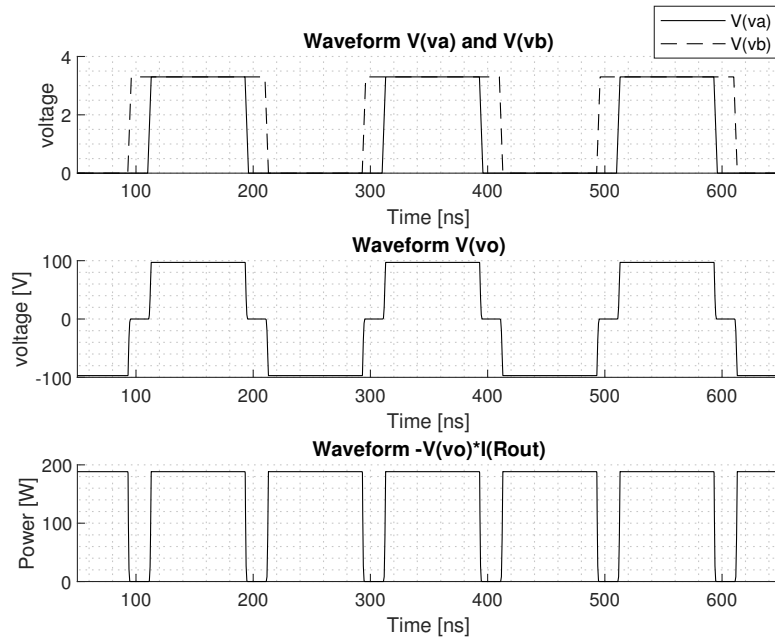


Figure 3.13: LTspice simulation output of transmitter with level shifter and half-bridge power stage from fig. B.1

simulation of the power stage was implemented where the full model can be seen in fig. B.1. The resulting waveforms are seen in fig. 3.13. In the top subplot, the input voltages INA and INB are seen with their dead-time visible on each overlapped on period. Since INB is driving an N-channel metal-oxide-semiconductor field-effect transistor (*MOSFET*), the driving pulse-train should be thought of having the opposite polarity. When looking at the middle subplot, it is noted that dead-time is visible as the time where the output voltage is zero. Thus, during that time neither field-effect transistor (*FET*) are allowing a current to pass, and therefore the voltage across the load is equal to zero. The lower subplot shows the maximum ideal power delivery using the peak pulse voltage, assuming the load is equal to 50Ω . In reality, due to the equipment available for testing, the pulse peak voltage will be less than 100 V.

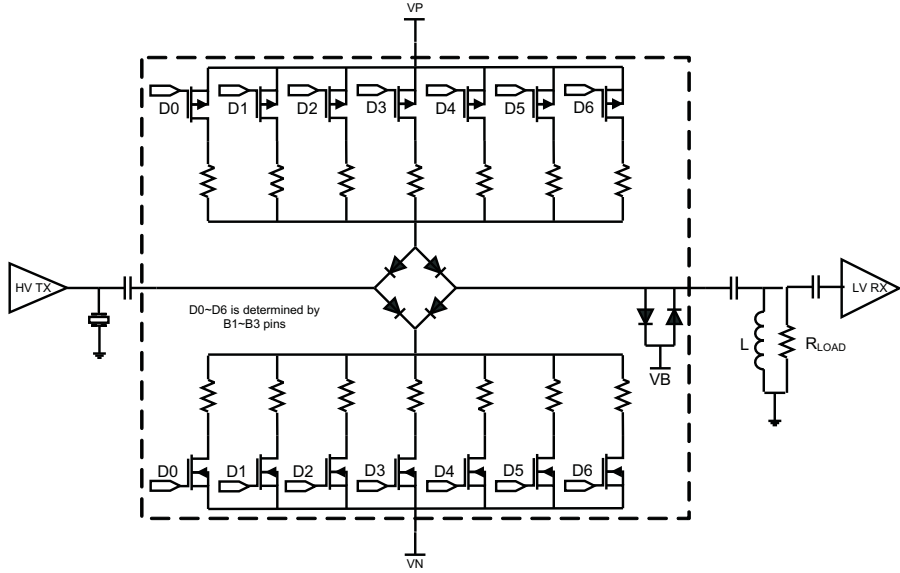


Figure 3.14: Block diagram of TX/RX switching circuit where the inputs D1 through D6 are binary decoded from inputs B_1, B_2, B_3 [25]

3.4 Transmit/Receive Switch

Among the design considerations for the transmit and receive switch were the TX810[25] and MD0101[51]. Both ICs are acceptable choices, however the MD0101 is a newer and generally better choice since it has a lower insertion loss, which means that less of the ultrasound signal is lost as it passes through the switch. This results in a higher quality image with better signal-to-noise ratio. Additionally, MD0101 has a wider bandwidth, which means that it can transmit and receive ultrasound signals over a broader range of frequencies. However, since the TX810 is in stock and is also acceptable, it was chosen for the design. TX810 is an IC from Texas Instruments that can be used to switch transmit and receive paths of an ultrasound system. The IC fundamentally works by having a 3-bit programmable pin interface that will open and close the switch with a variable bias current. See fig. 3.15 for a visualisation of the switching operation, where INPUT is the incoming Doppler waveform being picked up from the transducer, $B_3/B_2/B_1$ is the switching signal closing the switch and thereby going in receive mode, and OUTPUT is the received signal seen in the AFE. The TX810 can switch the transmit and receive paths for up to 8 different

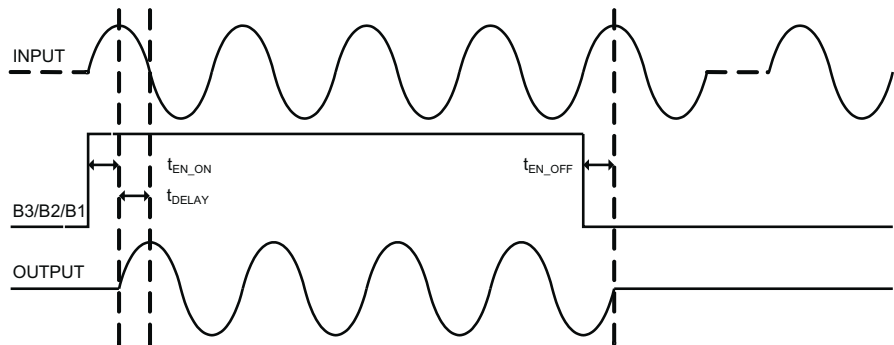


Figure 3.15: Timing diagram of switching interface where $t_{EN_ON} = 0.6 \mu s$, $t_{EN_OFF} = 2.4 \mu s$, and $t_{DELAY} = 1.3 \text{ ns}$ for the condition $B_1 = B_2 = B_3$ [25]

transducers at the same time. The TX810 is programmed to switch the transmit and receive paths at specific times, as determined by the user. For example, the user can program the TX810 to switch the transmit and receive paths of a particular transducer at a specific time during the ultrasound examination. The IC is typically used in conjunction with an ultrasound system and one or more transducers. Transducers are used to transmit and receive ultrasound waves, which are used to generate images of the body's internal structures. The TX810 is used to switch the transmit and receive paths for each transducer at the appropriate times, allowing the ultrasound system to capture images from multiple angles simultaneously. When high-voltage transmitter signals are applied to the input, the internal diodes limit the output voltage. While in receive mode, the TX810's insertion loss is minimized. The TX810 features a 3-bit interface that may be used to program bias current from 7 mA to 0 mA for varying performance and power requirements, unlike conventional T/R switches. The device is put up in power-down mode when the TX810 bias current is set to 0 mA (high-impedance mode). The TX810 does not put significant load on high-voltage transmitters when operating in the high-impedance mode. A PCB design was implemented in Altium Designer [59] utilising three channels of the maximum eight available channels in the IC. Seen in fig. 3.16 is a 3D render of the designed PCB. The module is designed with three usable channels, either three separate transducers for

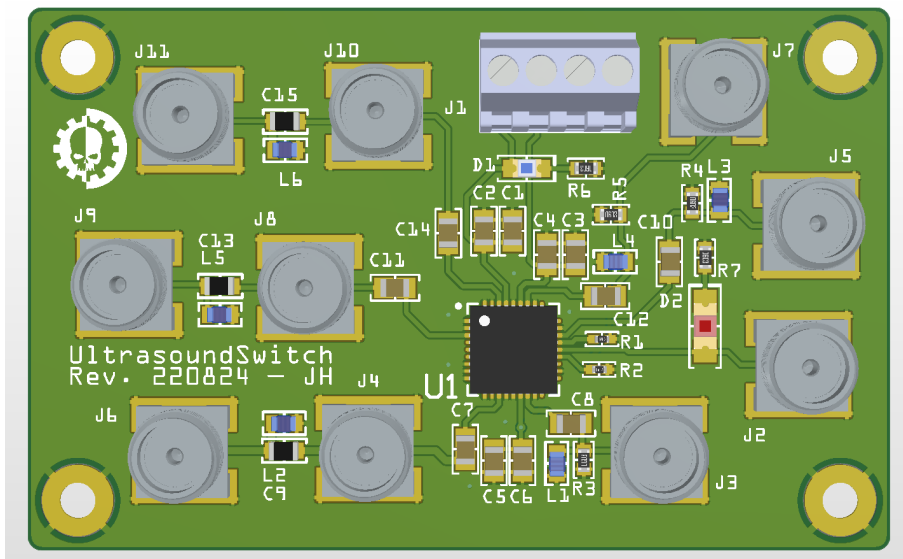


Figure 3.16: 3D Render of PCB in Altium Designer

multi-angle sonography, or a capacitive micromachined ultrasound transducer (*CMUT*) with three channels in a single angle. However, the following experiments with the TX/RX switch, only one channel will be used for simplifying the data acquisition experiments.

3.5 Band-Pass Filter

After the signal is received, it is filtered with a *BP* filter to remove unwanted noise and interference from the received signal. The presence of these unwanted frequency components can distort the received signal and reduce the quality of the resulting imaging. The specs from the datasheet [47] are seen in fig. 3.17. Filtering the received signal through this device means that any signals produced by the transducer at frequencies outside the range of interest will be attenuated. An ultrasound receiver requires a band-pass filter to enable only the frequencies within a predetermined range to pass through, while blocking out

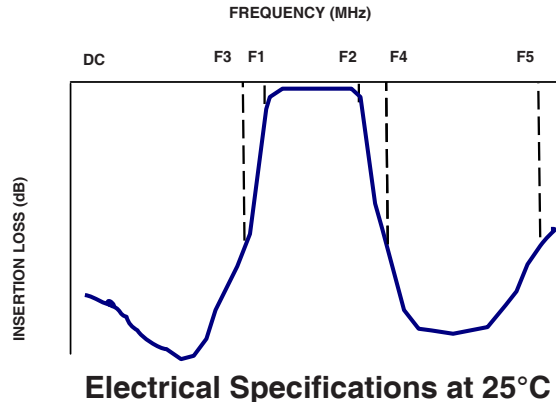


Figure 3.17: Band-Pass Filter with (above) insertion loss showing a pass band of 2 MHz to 7 MHz of 0.5 dB insertion loss and (below) electrical specifications showing the minimum stop band attenuation of 20 dB

frequencies outside that range.

3.6 Preamplifier

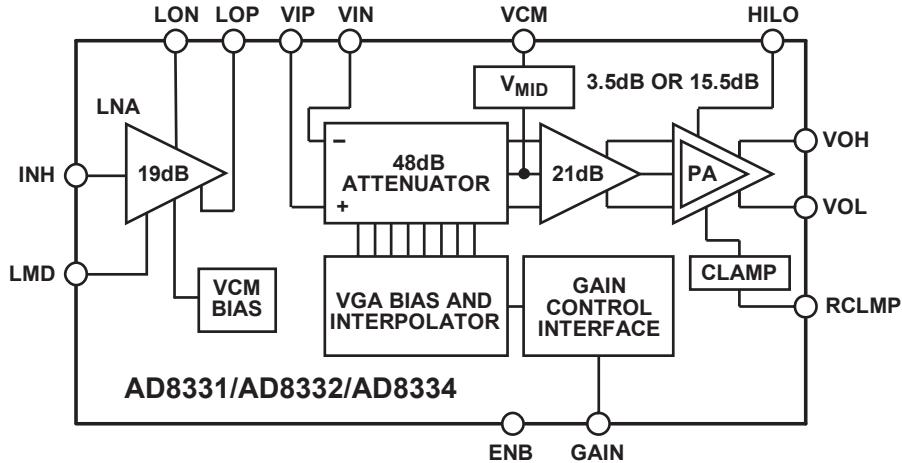


Figure 3.18: Block diagram of preamplifier AD8332 [41]

The isolated signal is still rather weak to be measured using digital circuits, and therefore the amplitude must be increased with the preamplifier circuit. This circuit is based on the integrated circuit from Analog Devices AD8332 [41], which is a device that combines a dual-channel *LNA* and *VGA*, designed specifically for ultrasound systems. A diagram of its internal functional blocks can be seen in fig. 3.18. The AD8332 functions at frequencies up to 120 MHz. Each channel includes an ultralow noise preamp (*LNA*), a *VGA* with 48 dB of gain range, and a selectable gain postamp with adjustable output limiting. The

LNA gain is 19 dB with a single-ended input and differential outputs. To match the signal source without sacrificing noise performance, the LNA input impedance can be adjusted using a single resistor. The VGA has low output-referred noise, which is useful in driving high-speed differential ADCs. The gain of the postamp can be pin-selected to 3.5 dB or 15.5 dB, depending on the converter requirements. The output can be limited to a user-defined clamping level to avoid input overload to a subsequent *ADC*, with the clamping level adjusted using an external resistor. A SPICE macromodel is provided by the vendor and the preamplification is successfully simulated using LTspice with the full LTspice model found in fig. B.2, and the probed inputs and outputs seen in fig. 3.19.

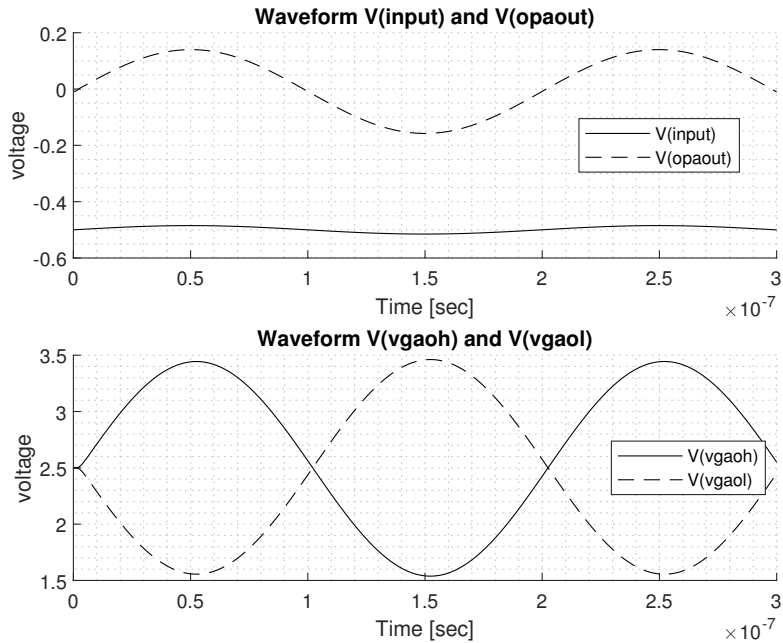


Figure 3.19: LTspice simulation output of preamplifier *LNA* and *VGA* from fig. B.2

3.7 Quadrature Demodulator

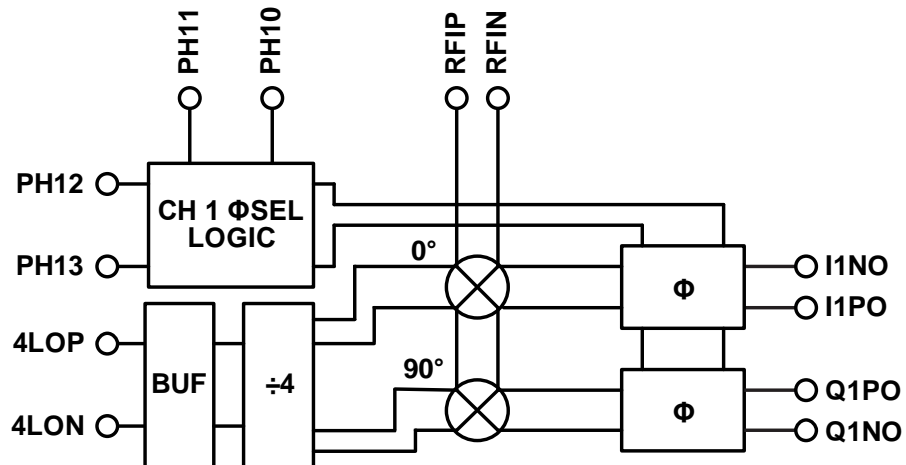


Figure 3.20: Block diagram of demodulator AD8333 [42]

After the preamplifier, the amplified signal must be demodulated to prepare it for sampling.

The device used for quadrature demodulation is an integrated circuit from Analog Devices AD8333 [42] I/Q demodulator. A diagram of the internal functional blocks can be seen in fig. 3.20 where the primary inputs are RFIP and RFIN, which are the two differential RF signals from the preamplifier. The RF inputs connect directly to the outputs of the LNA of the preamplifier. The internal 0° and 90° phases of the local oscillator (LO) are generated by a divide-by-4 circuit that drives the mixers of a matched I/Q demodulator pair. The I and Q outputs are presented as currents, making summation possible. The summed current outputs are then converted to voltages by a high dynamic range, current-to-voltage (I-V) converter, such as the AD8021 [18], which functions as a transimpedance amplifier. A SPICE macromodel is provided by the vendor and the I/Q demodulation is successfully simulated using LTspice using the LTspice model found in appendix fig. B.3, with the probed inputs and outputs seen in figs. 3.21 and 3.22.

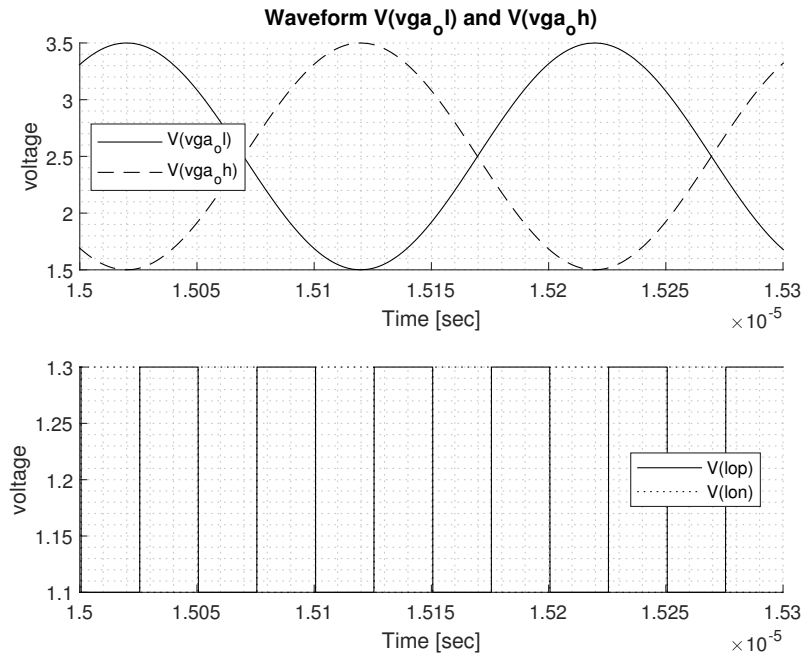


Figure 3.21: LTspice simulation demodulator input variables from fig. B.3

3.8 Sample and Hold

In this system, the sample-and-hold amplifier is necessary to keep values between each sample line. In chapter 2, it was described how the pulsed-wave flow-meter measures the movement of scatterers by sampling the back-scattered signal at a specific depth. Generally, the intended use for this part is in general data acquisition systems such as an *ADC*. In that application, the sample-and-hold amplifier captures an analog signal and retains it during certain operations, usually analog-to-digital conversion. Through a S/H input, two possible modes are selected, *sample* or *hold*. During the sample mode of operation, the output of the sample-and-hold amplifier follows the input. During the hold mode of operation, the output may not change by more than 1 least significant bit (*LSB*). The typical usage of a SHA is to keep the ADC input constant throughout the conversion process. With some types of ADCs, but not all, the input cannot change by more than 1 *LSB* during the conversion, or else the process will be compromised. This can either impose very low frequency limits on such ADCs or necessitate their use with a SHA to hold the input during each conversion. An internal capacitor forms the key component of the sample-and-hold

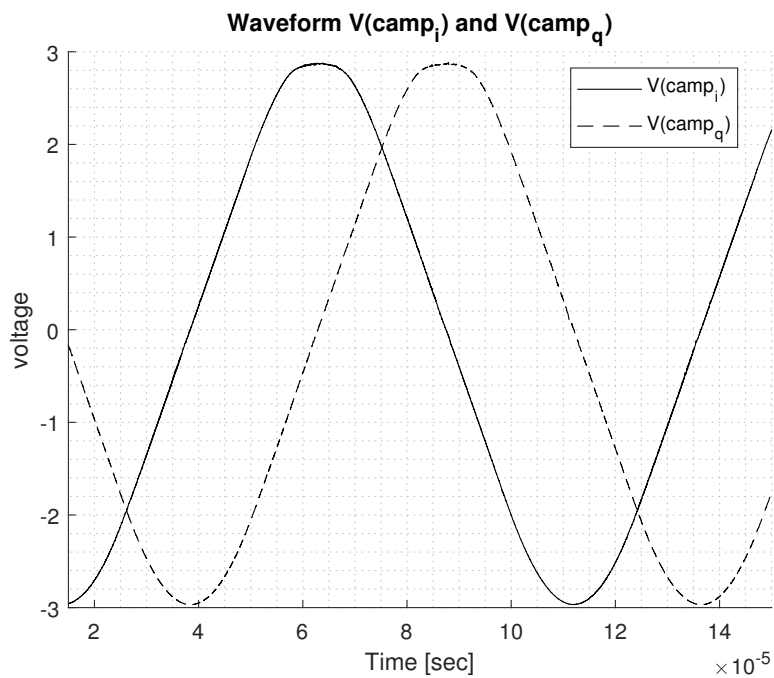


Figure 3.22: LTspice simulation demodulator output variables Q and I voltages from fig. B.3

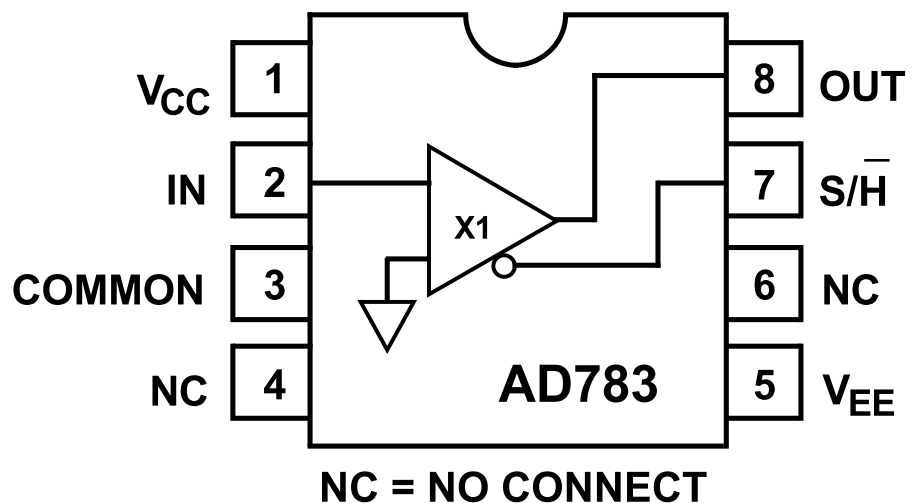


Figure 3.23: AD783 Sample and Hold Amplifier functional block diagram [34]

amplifier, which serves as the energy storage device. The input amplifier buffers the input signal by presenting a high impedance to the signal source, while providing current gain to charge the hold capacitor. In the sample mode, the voltage on the hold capacitor follows the input signal, albeit with some delay and bandwidth limitations. In the hold mode, the switch is opened, and the capacitor retains the voltage present before being disconnected from the input buffer. The output buffer prevents the held voltage from discharging too soon by offering a high impedance to the hold capacitor. The switching circuit and its driver work together to enable the SHA to alternate between sample and hold modes.

In the pulsed-wave flowmeter, the sample-and-hold amplifier is used to keep each sample value between each gate pulse. This is done for both the I and Q signals in parallel. A diagram of a sample-and-hold operation can be seen in fig. 3.24.

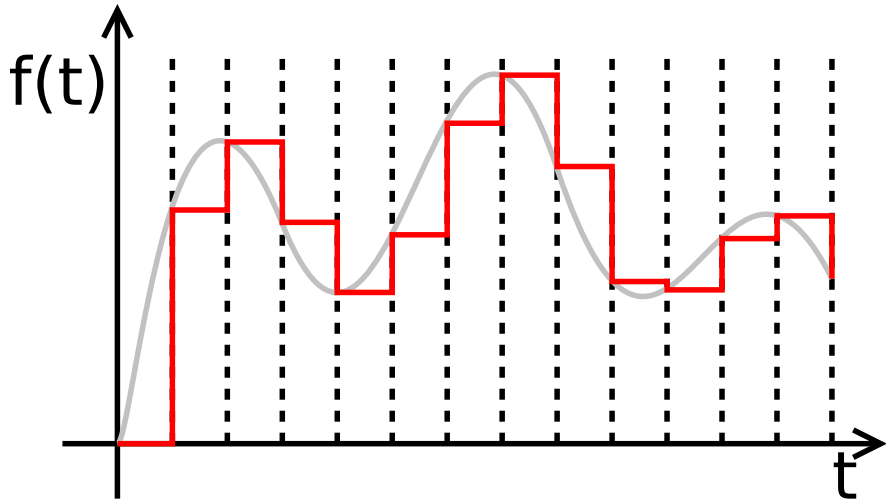


Figure 3.24: Sample and Hold function with input function $f(t)$ over time [62]

3.9 Pulse-Repetition, Wall Filter, DC-Coupling

Finally, the signal should be DC coupled for sampling. Combined with this circuit, a high-pass (*HP*) filter is used as a combined pulse repetition frequency (*PRF*) and Wall-filter in conjunction with a 2 dB gain amplification to maximize dynamic range of the *ADC* measurements from 0 V to 3.3 V. A SPICE simulation was implemented and a small signal analysis as well as a transient analysis was conducted. The resulting small signal analysis can be seen in fig. 3.25 and the transient analysis can be seen in fig. 3.26.

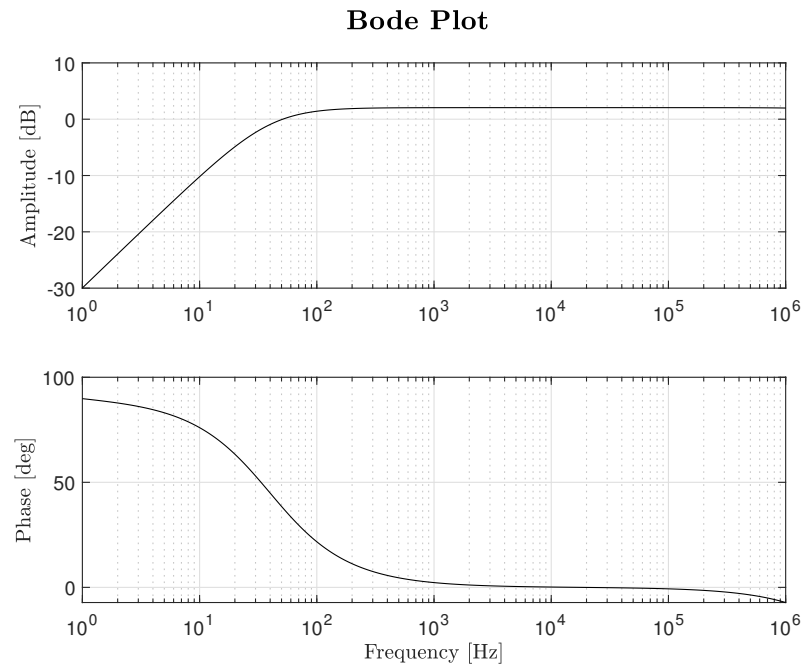


Figure 3.25: Small-signal analysis of DC-Coupling filter circuit

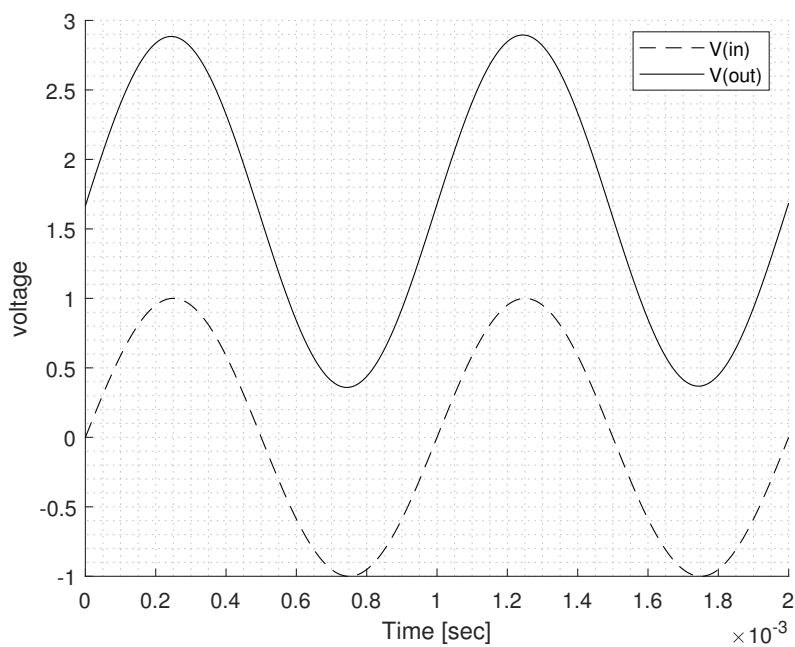


Figure 3.26: Transient analysis of DC-Coupling filter circuit

4 Production

In this chapter, the steps involved in turning a theoretical design into a tangible system will be outlined. Since the synthesis chapter dealt with explanations of the functions of each module and simulations, with a subsequent evaluation of the outcomes, this chapter will focus on the creation of physical hardware setups and reproducing the desired results using lab experiments. As such, each module will be tested independently to validate its function before a larger, more comprehensive experiment is conducted.

4.1 Control System

4.2 Power Stage

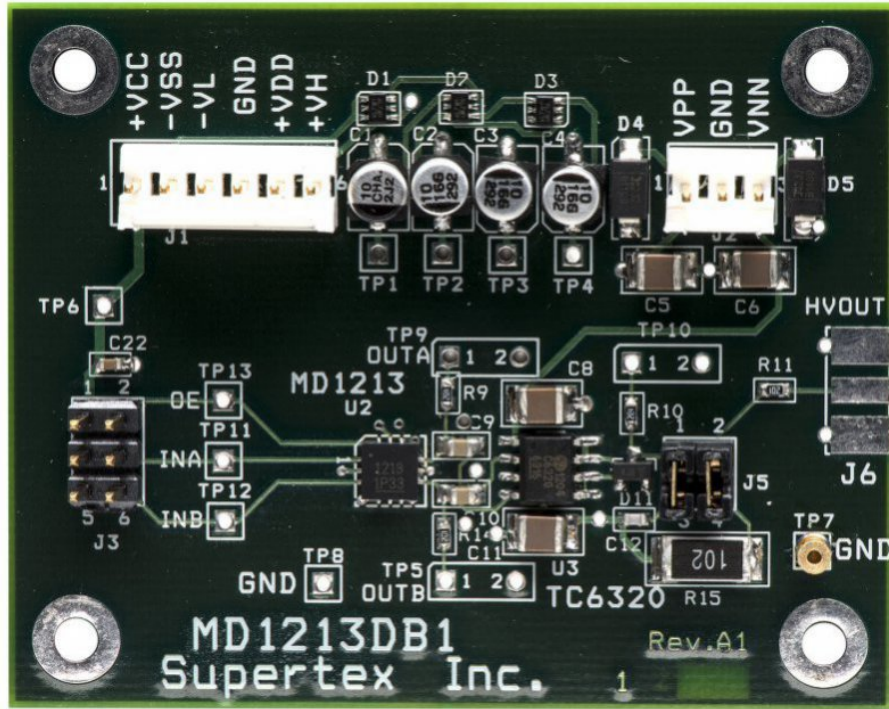


Figure 4.1: MD1213DB1 High Speed Pulser

A picture of the power stage PCB can be seen in fig. 4.1. An experiment is conducted to validate the function of the power stage. Using the jumpers, the PCB is configured without its onboard load, and a *PZT* transducer is attached with a splitter adapter to connect the other side to an oscilloscope for data acquisition. Seen in fig. 4.2 are actual measured inputs and outputs of the power stage. On the input, there are two complementary 5 MHz signals with varying duty cycle to generate the desired dead-time. On the output, we see the rail-to-rail push-pull operation of the *MOSFET* half-bridge. The schematic of the transmitter can be found in the appendix in ???. Noticeable noise is observed in the input signal top and base, but is negligible for the successful operation. Possibly, the noise is due to a cable and adapter problem.

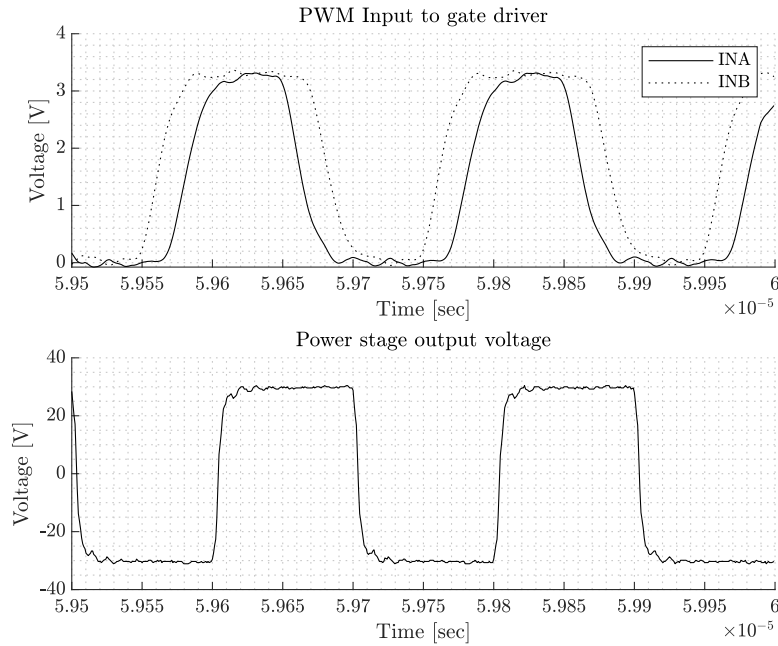


Figure 4.2: Measured input and output of power stage PCB. (Above) Input to gate driver with dead-time (Below) Output of MOSFET half-bridge and the voltage across the load

4.3 Transmit/Receive Switch

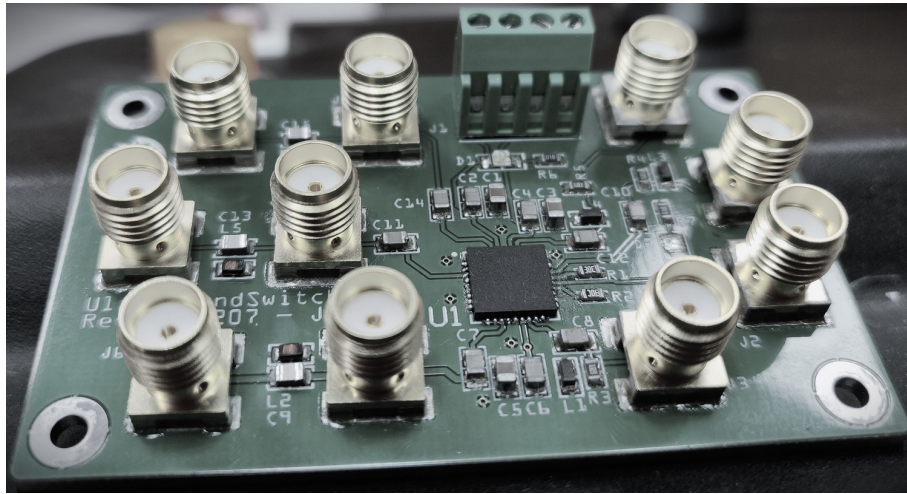


Figure 4.3: Transmit/Receive Switch after assembly

The entire schematic of the transmit/receive switch can be found in the appendix in ??. As mentioned in the previous chapter, a PCB layout was made and a batch of 5 was ordered with an accompanying stencil for fast assembly. After the PCBs arrived, the stencil was mounted in the stencil frame and the PCB aligned for solder paste application. After solder paste application is completed, all the components are placed on their corresponding footprints and the PCB is placed in the reflow oven. The equipment used in this process is listed in table C.1. The finished assembly can be seen in fig. 4.3. For validating the TX/RX switch, an experiment is conducted with a *PZT* transducer, water tank, function generator and an oscilloscope. Using two input signals, $f_{\text{pref}} = 10 \text{ kHz}$ switch signal, and $f_0 = 5 \text{ MHz}$



Figure 4.4: TX/RX Switch reflection experiment with water tank

burst mode transmit signal, the switch is configured to transmit and receive. A picture of the submerged transducer with a reflector can be seen in fig. 4.4. After submerging the transducer in distilled water and measuring on the receiver side of the TX/RX switch, a reflected signal from the tank can be observed in fig. 4.5.

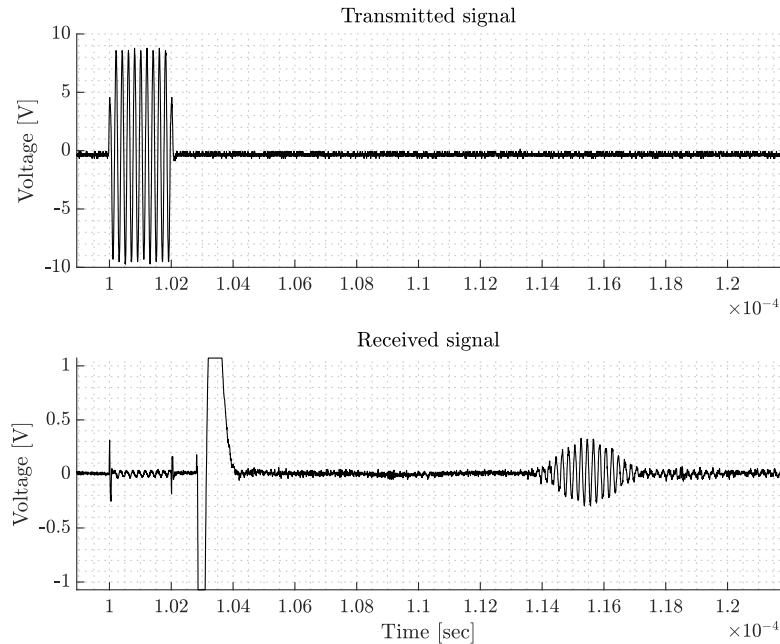


Figure 4.5: Measured transmit and receive on Transmit/Receive Switch PCB (Above)
Measured transmit voltage (Below) Received reflected signal off water tank

4.4 Band-Pass Filter

As the band-pass filter was described in the previous chapter, it is desired to validate its frequency response to determine if it lives up to its function. To obtain the frequency response, a bode plot of the magnitude and phase is measured from 300 kHz until 20 MHz using a vector network analyzer (*VNA*) in a S21 configuration, meaning a measurement of the output in respect to the input. This measurement determines the difference in magnitude and phase of the output in comparison with the input signal. Observed in fig. 4.6 is the frequency response of the band-pass filter measured on a *VNA*. It is noted that the pass band frequencies are mostly as expected with -0.5 dB frequencies at 1.5 MHz and 7 MHz. Though, the roll-off in the higher stop band appears somewhat lower than the lower stop-band. That would mean that more higher frequency noise components are retained than in the lower stop band. For the phase, it seems to have a significant phase delay, going from around 100° to 250° from the start to the end of the pass band.

4.5 Preamplifier

Before the signal can be demodulated, it must be DC-biased and amplified. This is what the preamplifier is for. For the preamplifier, the circuit is validated using an experiment where a function generator is transmitting a low amplitude sine with ac-coupling and measure the amplified dc-coupled output. Seen in fig. 4.7 are measurements of the preamplifier

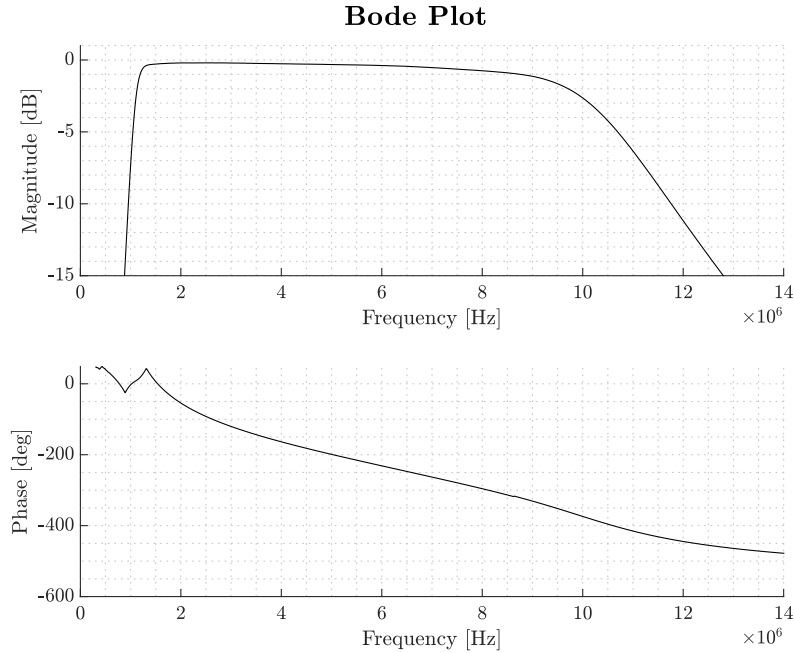


Figure 4.6: Band-pass Filter bode plot from 0.3 MHz to 14 MHz with (above) magnitude and (below) phase

circuits showing a 70 mV input signal and a 300 mV output signal with a 2.5 V DC bias. In this application, however, only the *LNA* is used, and the *VGA* is bypassed in the hardware preamplifier configuration. The schematic of the preamplifier circuit is part of the demodulation schematic and can be found in the appendix in ??.

4.6 Quadrature Demodulator

As described in the previous chapter, the demodulator uses a I/Q quadrature demodulation scheme to take two differential RF signals and a quadruple frequency signal, in this case 5 MHz and 20 MHz, respectively, and determines the frequency difference between the fundamental frequency and the Doppler frequency on the output. Seen in fig. 4.9 are the input signals, differential signals of 5.001 MHz and 20 MHz local oscillator signal. Seen in fig. 4.10 are the demodulated output signals *I* and *Q*, where the phase between *I* and *Q* denotes the Doppler shift direction, or rather, the direction of flow of the scatterer. The entire schematic of the demodulator can be found in the appendix in ??.

4.7 Sample and Hold

After each demodulated burst is sampled, between each sample line pulse repetition it is desired to hold the voltage, so the analogue-to-digital conversion that may be running asynchronously does not sample zero-values between the bursts. Therefore, an experiment is conducted with the sample-and-hold amplifier to verify the functionality. A low frequency I-Q simulated signal is created from the function generator with a sample gating pulse train to control the sample-and-hold function. Seen in fig. 4.11 is the measured inputs and outputs of the circuit during the experiment. Above is the I-Q input and in the middle is the sample gating, and below is the output signal. On the output signal, it is noted the corresponding voltage transients for every pulse in the gate input.

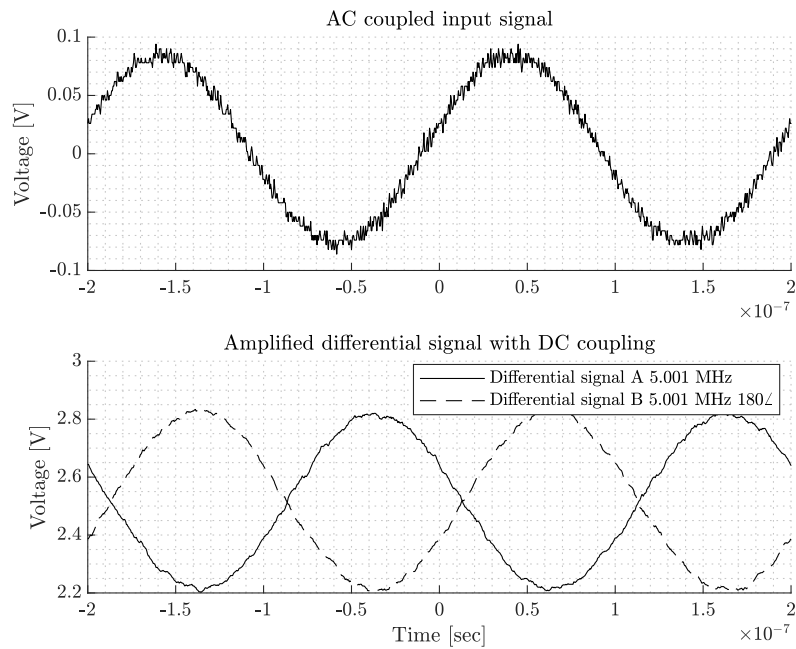


Figure 4.7: Measured input of preamplifier PCB, (Above) AC coupled input signal with amplitude 1 V (Below Measured output of preamplifier PCB, Differential signal with DC coupling and $\times 19$ dB amplification)

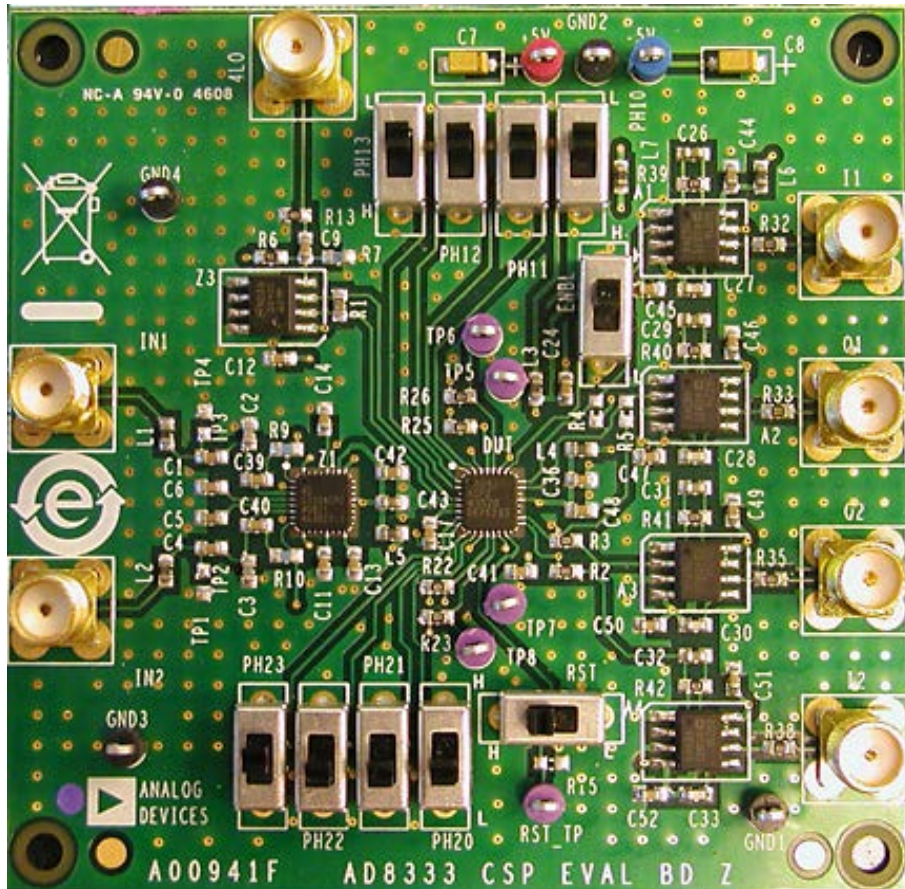


Figure 4.8: Demodulator PCB AD8333-EVALZ

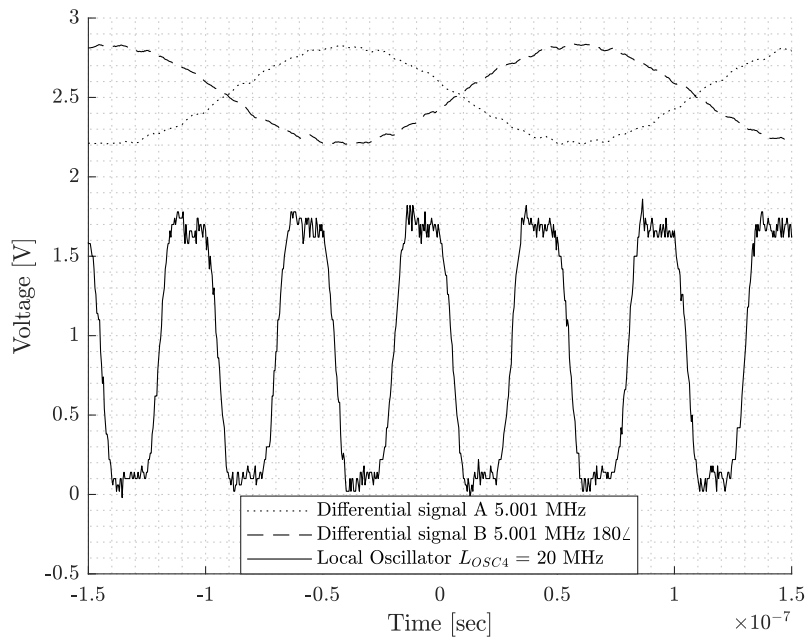


Figure 4.9: Measured input of demodulator PCB (Above) Input from received signal (Below) Input from local oscillator ($f_0 \cdot 4$)

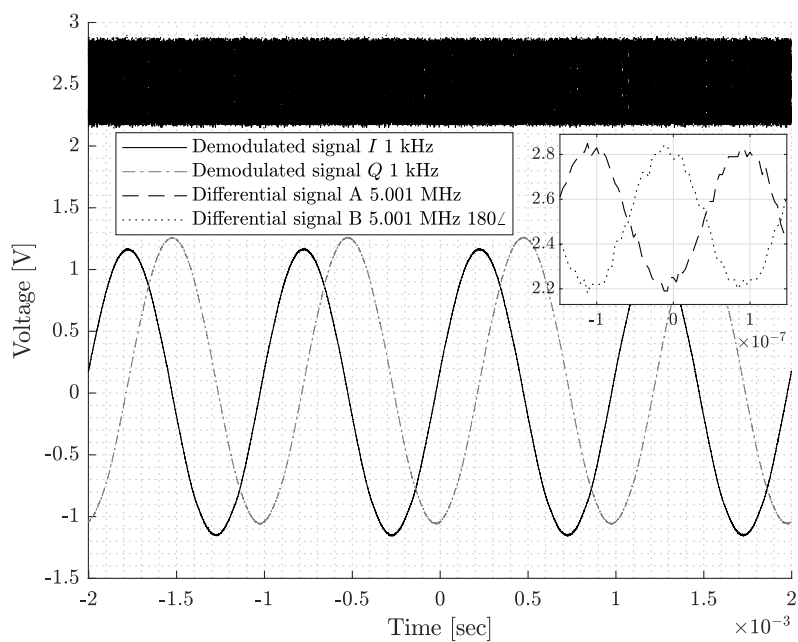


Figure 4.10: Measured output of demodulator PCB

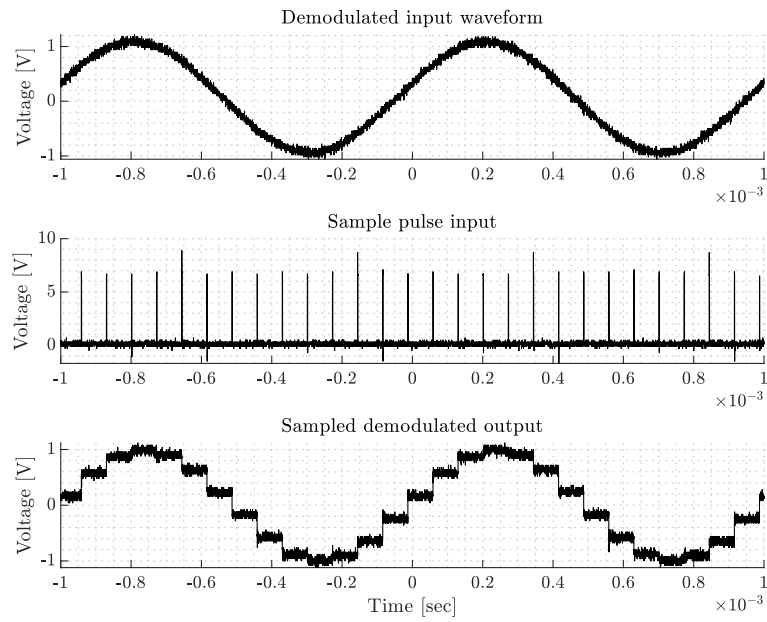


Figure 4.11: Measured input and output of Sample and Hold amplifier

4.8 Pulse-Repetition and Wall Filter

4.9 Digital Signal Processor

5 Conclusion

Conclude?

5.1 Future Work

Blah

Bibliography

- [1] S. Satomura, T. Yoshida, M. Mori, Y. Nimura, G.-i. Hikita, S. Takagishi, and K. Nakanishi, “Analysis of heart motion with ultrasonic Doppler method and its clinical application”, *American Heart Journal*, vol. 61, pp. 61–75, 1 January 1961, ISSN: 00028703. DOI: 10.1016/0002-8703(61)90517-8. [Online]. Available: <https://linkinghub.elsevier.com/retrieve/pii/0002870361905178>.
- [2] D. Baker, “Pulsed Ultrasonic Doppler Blood-Flow Sensing”, *IEEE Transactions on Sonics and Ultrasonics*, vol. 17, pp. 170–184, 3 Jul. 1970, ISSN: 0018-9537. DOI: 10.1109/t-su.1970.29558. [Online]. Available: <http://ieeexplore.ieee.org/document/1538563/>.
- [3] K. K. Shung, R. A. Sigelmann, and J. M. Reid, “Scattering of Ultrasound by Blood”, *IEEE Transactions on Biomedical Engineering*, vol. Bme-23, pp. 460–467, 6 November 1976, ISSN: 0018-9294. DOI: 10.1109/tbme.1976.324604. [Online]. Available: <http://ieeexplore.ieee.org/document/4121084/>.
- [4] F. S. Schlindwein, M. J. Smith, and D. H. Evans, “Spectral analysis of Doppler signals and computation of the normalised first moment in real time using a digital signal processor”, *Medical & Biological Engineering & Computing*, vol. 26, pp. 228–232, 2 March 1988, ISSN: 0140-0118. DOI: 10.1007/bf02442271. [Online]. Available: <http://link.springer.com/10.1007/BF02442271>.
- [5] K. K. Shung and G. A. Thieme, *Ultrasonic scattering in biological tissues*. CRC Press, 1993, p. 499, ISBN: 9780849365683. [Online]. Available: <https://www.routledge.com/Ultrasonic-Scattering-in-Biological-Tissues/Shung-Thieme/p/book/9780849365683>.
- [6] T. Hall, “An improved wall filter for flow imaging of low velocity flow”, vol. 3, IEEE, October 1994, 1701–1704 vol.3, ISBN: 0-7803-2012-3. DOI: 10.1109/ultsym.1994.401918. [Online]. Available: <http://ieeexplore.ieee.org/document/401918/>.
- [7] L. Bessi, F. Guidi, F. Gucci, C. Atzeni, and P. Tortoli, “Single-channel digital demodulation of ultrasound bandpass signals for flow-imaging applications”, in Springer, Boston, MA, 1995, pp. 331–335. DOI: 10.1007/978-1-4615-1943-0_34. [Online]. Available: http://link.springer.com/10.1007/978-1-4615-1943-0_34.
- [8] J. A. Jensen, “An Analysis of Pulsed Wave Ultrasound Systems for Blood Velocity Estimation”, *Acoustical Imaging*, L. T. Piero and Masotti, Eds., pp. 377–384, 1996. DOI: 10.1007/978-1-4419-8772-3__61. [Online]. Available: <http://link.springer.com/10.1007/978-1-4419-8772-3%5C%5F61>.
- [9] I. Güler and Y. Sava, “Design parameters of pulsed wave ultrasonic Doppler blood flowmeter”, *Journal of Medical Systems*, vol. 22, pp. 273–278, 4 1998, ISSN: 01485598. DOI: 10.1023/a:1022665802010.
- [10] P. Wells, “Doppler studies of the vascular system”, *European Journal of Ultrasound*, vol. 7, pp. 3–8, 1 February 1998, ISSN: 09298266. DOI: 10.1016/s0929-8266(98)00006-8. [Online]. Available: <https://linkinghub.elsevier.com/retrieve/pii/S0929826698000068>.
- [11] P. J. Fish, “Ultrasonic investigation of blood flow”, *Proceedings of the Institution of Mechanical Engineers, Part H: Journal of Engineering in Medicine*, vol. 213, pp. 169–180, 3 March 1999, Pmid: 10420772. DOI: 10.1243/0954411991534898. [Online]. Available: <https://doi.org/10.1243/0954411991534898>.

- [12] P. R. Hoskins, “A review of the measurement of blood velocity and related quantities using Doppler ultrasound”, *Proceedings of the Institution of Mechanical Engineers, Part H: Journal of Engineering in Medicine*, vol. 213, pp. 391–400, 5 1999, Pmid: 10581966. DOI: 10.1243/0954411991535004. [Online]. Available: <https://doi.org/10.1243/0954411991535004>.
- [13] T. Jansson, H. W. Peresson, and K. Lindström, “Estimation of blood perfusion using ultrasound”, *Proceedings of the Institution of Mechanical Engineers, Part H: Journal of Engineering in Medicine*, vol. 213, pp. 193–193, 3 March 1999, ISSN: 0954-4119. DOI: 10.1243/0954411991534915. [Online]. Available: <http://journals.sagepub.com/doi/10.1243/0954411991534915>.
- [14] J. A. Jensen, “Algorithms for estimating blood velocities using ultrasound”, *Ultrasonics*, vol. 38, pp. 358–362, 1-8 March 2000, ISSN: 0041624x. DOI: 10.1016/s0041-624x(99)00127-4. [Online]. Available: <https://linkinghub.elsevier.com/retrieve/pii/S0041624X99001274>.
- [15] P. Munk, “Estimation of blood velocity vectors using ultrasound”, Technical University of Denmark, 2000. [Online]. Available: <https://findit.dtu.dk/en/catalog/537f0d537401dbcc1200be04>.
- [16] E. Picano, “Sustainability of medical imaging”, *BMJ*, vol. 328, pp. 578–580, 7439 March 2004, ISSN: 0959-8138. DOI: 10.1136/bmj.328.7439.578. [Online]. Available: <https://www.bmjjournals.org/lookup/doi/10.1136/bmj.328.7439.578>.
- [17] A. Erguri, Y. Huang, X. Zhuang, O. Oralkan, G. Yarahoglu, and B. Khuri-Yakub, “Capacitive micromachined ultrasonic transducers: Fabrication technology”, *IEEE Transactions on Ultrasonics, Ferroelectrics, and Frequency Control*, vol. 52, no. 12, pp. 2242–2258, 2005. DOI: 10.1109/TUFFC.2005.1563267.
- [18] *AD8021 Low Noise, High Speed Amplifier for 16-Bit Systems*, Analog Devices, Inc., May 2006. [Online]. Available: <https://www.analog.com/media/en/technical-documentation/data-sheets/AD8021.pdf>.
- [19] E. Chérin, R. Williams, A. Needles, G. Liu, C. White, A. S. Brown, Y.-Q. Zhou, and F. S. Foster, “Ultrahigh frame rate retrospective ultrasound microimaging and blood flow visualization in mice *in vivo*”, *Ultrasound in Medicine & Biology*, vol. 32, pp. 683–691, 5 May 2006, ISSN: 03015629. DOI: 10.1016/j.ultrasmedbio.2005.12.015. [Online]. Available: <https://linkinghub.elsevier.com/retrieve/pii/S0301562906000172>.
- [20] *EL7104 High Speed, Single Channel, Power MOSFET Driver*, Renesas Electronics, Jun. 2006. [Online]. Available: <https://www.renesas.com/us/en/document/dst/el7104-datasheet>.
- [21] I. K. H. Tsang, B. Y. S. Yiu, D. K. H. Cheung, H. C. T. Chiu, C. C. P. Cheung, and A. C. H. Yu, “Design of a multi-channel pre-beamform data acquisition system for an ultrasound research scanner”, IEEE, Sep. 2009, pp. 1840–1843, ISBN: 978-1-4244-4389-5. DOI: 10.1109/ultsym.2009.5441869. [Online]. Available: <http://ieeexplore.ieee.org/document/5441869/>.
- [22] E. A. Aydn and . Güler, “Design Of Pic-controlled Pulsed Ultrasonic Transmitter For Measuring Gingiva Thickness”, *Instrumentation Science & Technology*, vol. 38, pp. 411–420, 6 October 2010, ISSN: 1073-9149. DOI: 10.1080/10739149.2010.509149. [Online]. Available: <http://www.tandfonline.com/doi/abs/10.1080/10739149.2010.509149>.
- [23] P. R. Hoskins, “Haemodynamics and blood flow measured using ultrasound imaging”, *Proceedings of the Institution of Mechanical Engineers, Part H: Journal of Engineering in Medicine*, vol. 224, pp. 255–271, 2 February 2010, Pmid: 20349818, ISSN: 0954-4119.

- DOI: 10.1243/09544119jeim572. [Online]. Available: <http://journals.sagepub.com/doi/10.1243/09544119JEIM572>.
- [24] N. Matsuoka, D.-G. Paeng, R. Chen, H. Ameri, W. Abdallah, Q. Zhou, A. Fawzi, K. K. Shung, and M. Humayun, “Ultrasonic Doppler measurements of blood flow velocity of rabbit retinal vessels using a 45-MHz needle transducer”, *Graefe's Archive for Clinical and Experimental Ophthalmology*, vol. 248, pp. 675–680, 5 2010, ISSN: 1435-702x. DOI: 10.1007/s00417-009-1298-9. [Online]. Available: <https://doi.org/10.1007/s00417-009-1298-9>.
- [25] *TX810 8-Channel, Programmable T/R Switch for Ultrasound*, Texas Instruments, April 2010. [Online]. Available: <https://www.ti.com/lit/gpn/tx810>.
- [26] K. L. Hansen, M. B. Nielsen, and J. A. Jensen, “In-vivo studies of new vector velocity and adaptive spectral estimators in medical ultrasound”, 2011. [Online]. Available: <https://orbit.dtu.dk/en/publications/in-vivo-studies-of-new-vector-velocity-and-adaptive-spectral-estimator>.
- [27] J. A. Jensen, S. I. Nikolov, J. Udesen, et al., “Recent advances in blood flow vector velocity imaging”, IEEE, October 2011, pp. 262–271, ISBN: 978-1-4577-1252-4. DOI: 10.1109/ultsym.2011.0064. [Online]. Available: <http://ieeexplore.ieee.org/document/6293382/>.
- [28] A. Sarvazyan, T. J. Hall, M. W. Urban, M. Fatemi, S. R. Aglyamov, and B. S. Garra, “An Overview of Elastography-An Emerging Branch of Medical Imaging”, *Current Medical Imaging Reviews*, vol. 7, pp. 255–282, 4 November 2011, ISSN: 15734056. DOI: 10.2174/157340511798038684. [Online]. Available: <http://www.eurekaselect.com/openurl/content.php?genre=article%5C&issn=1573-4056%5C&volume=7%5C&issue=4%5C&spage=255>.
- [29] T. A. Bigelow, A. Kellar, A. Tapia, F. Ferrer, J. Batcheler, J. Driggs, and R. Page, “Design Document for a Pulse Echo Ultrasound System”, Iowa State University, December 2012.
- [30] C.-C. Huang, P.-Y. Lee, P.-Y. Chen, and T.-Y. Liu, “Design and implementation of a smartphone-based portable ultrasound pulsed-wave doppler device for blood flow measurement”, *IEEE Transactions on Ultrasonics, Ferroelectrics and Frequency Control*, vol. 59, pp. 182–188, 1 January 2012, ISSN: 0885-3010. DOI: 10.1109/tuffc.2012.2171. [Online]. Available: <http://ieeexplore.ieee.org/document/6138742/>.
- [31] C. A. Winckler, P. R. Smith, D. M. J. Cowell, O. Olagunju, and S. Freear, “The design of a high speed receiver system for an ultrasound array research platform”, Ieee, October 2012, pp. 1481–1484, ISBN: 978-1-4673-4562-0. DOI: 10.1109/ultsym.2012.0370. [Online]. Available: <http://ieeexplore.ieee.org/document/6562380/>.
- [32] J. A. Jensen, *Estimation of Blood Velocities Using Ultrasound: A Signal Processing Approach*, Third Edition. Department of Electrical Engineering, Technical University of Denmark, August 2013, ISBN: 9780521464840.
- [33] E. Pirnia, “Blood velocities estimation using ultrasound”, Lund University, Sep. 2013.
- [34] *AD783 Complete Very High Speed Sample-and-Hold Amplifier*, Analog Devices, October 2014. [Online]. Available: <https://www.analog.com/media/en/technical-documentation/data-sheets/AD783.pdf>.
- [35] J. E. Browne, “A review of doppler ultrasound quality assurance protocols and test devices”, *Physica Medica*, vol. 30, no. 7, pp. 742–751, 2014, ISSN: 1120-1797. DOI: <https://doi.org/10.1016/j.ejmp.2014.08.003>. [Online]. Available: <https://www.sciencedirect.com/science/article/pii/S1120179714005171>.

- [36] *MD1213DB1 High Speed ±100V 2A Pulser*, Supertex, Inc., March 2014. [Online]. Available: <https://ww1.microchip.com/downloads/en/DeviceDoc/md1213db1.pdf>.
- [37] R. K. Sagdiev, E. S. Denisov, Y. K. Evdokimov, M. G. Fazlyyyakhmatov, and N. F. Kashapov, “Phased array based ultrasound scanning system development”, *IOP Conference Series: Materials Science and Engineering*, vol. 69, p. 012012, 1 December 2014, ISSN: 1757-899x. DOI: 10.1088/1757-899x/69/1/012012. [Online]. Available: <https://iopscience.iop.org/article/10.1088/1757-899X/69/1/012012>.
- [38] T. L. Szabo, *Diagnostic Ultrasound Imaging: Inside Out*, Second Edition. Elsevier, 2014, ISBN: 9780123964878. DOI: 10.1016/c2011-0-07261-7. [Online]. Available: <https://linkinghub.elsevier.com/retrieve/pii/C20110072617>.
- [39] K. K. Shung, *Diagnostic Ultrasound: Imaging and Blood Flow Measurements*, Second Edition. CRC Press, December 2015, ISBN: 978-1-4665-8264-4.
- [40] L. Svilainis, A. Chazachmetovas, and V. Dumbrava, “Half bridge topology 500 V pulser for ultrasonic transducer excitation”, *Ultrasonics*, vol. 59, pp. 79–85, May 2015, ISSN: 0041624x. DOI: 10.1016/j.ultras.2015.01.014. [Online]. Available: <https://linkinghub.elsevier.com/retrieve/pii/S0041624X15000165>.
- [41] *AD8332 Ultralow Noise VGAs with Preamplifier and Programmable R_{IN}*, Analog Devices, May 2016. [Online]. Available: https://www.analog.com/media/en/technical-documentation/data-sheets/AD8331_8332_8334.pdf.
- [42] *AD8333 DC to 50 MHz, Dual I/Q Demodulator and Phase Shifter*, Analog Devices, May 2016. [Online]. Available: <https://www.analog.com/media/en/technical-documentation/data-sheets/AD8333.pdf>.
- [43] P. Govindan, B. Wang, P. Ravi, and J. Saniie, “Hardware and software architectures for computationally efficient three-dimensional ultrasonic data compression”, *IET Circuits, Devices & Systems*, vol. 10, pp. 54–61, 1 January 2016, ISSN: 1751-858x. DOI: 10.1049/iet-cds.2015.0083. [Online]. Available: <https://onlinelibrary.wiley.com/doi/10.1049/iet-cds.2015.0083>.
- [44] B. Wang and J. Saniie, “Ultrasonic Signal Acquisition and Processing platform based on Zynq SoC”, vol. 2016-August, IEEE, May 2016, pp. 0448–0451, ISBN: 978-1-4673-9985-2. DOI: 10.1109/eit.2016.7535282. [Online]. Available: <http://ieeexplore.ieee.org/document/7535282/>.
- [45] *MD1213 High-Speed Dual-MOSFET Driver*, Microchip Technology, Inc., Jun. 2017. [Online]. Available: <https://ww1.microchip.com/downloads/en/DeviceDoc/20005713B.pdf>.
- [46] S. Ricci and V. Meacci, “Data-adaptive coherent demodulator for high dynamics pulse-wave ultrasound applications”, *Electronics 2018, Vol. 7, Page 434*, vol. 7, p. 434, 12 December 2018, ISSN: 2079-9292. DOI: 10.3390/ELECTRONICS7120434. [Online]. Available: <https://www.mdpi.com/2079-9292/7/12/434/htm%20https://www.mdpi.com/2079-9292/7/12/434>.
- [47] *BPF-C4R5+ Bandpass Filter 50Ω 2 to 7 MHz*, Mini-Circuits, August 2019. [Online]. Available: <https://www.minicircuits.com/pdfs/BPF-C4R5+.pdf>.
- [48] B. Wang and J. Saniie, “A High Performance Ultrasonic System for Flaw Detection”, IEEE, October 2019, pp. 840–843, ISBN: 978-1-7281-4596-9. DOI: 10.1109/ultsym.2019.8926280. [Online]. Available: <https://ieeexplore.ieee.org/document/8926280/>.
- [49] H. Ding, D. Yang, J. Xu, X. Chen, X. Le, Y. Wang, L. Lin, and J. Xie, “Pulsed Wave Doppler Ultrasound Using 3.7 MHz Pmuts Toward Wearable Blood Flow Measurements”, IEEE, January 2020, pp. 400–403, ISBN: 978-1-7281-3581-6. DOI:

- 10 . 1109/mems46641 . 2020 . 9056430. [Online]. Available: <https://ieeexplore.ieee.org/document/9056430/>.
- [50] B. Jana, R. Biswas, P. K. Nath, G. Saha, and S. Banerjee, “Smartphone-Based Point-of-Care System Using Continuous-Wave Portable Doppler”, *IEEE Transactions on Instrumentation and Measurement*, vol. 69, pp. 8352–8361, 10 October 2020, ISSN: 0018-9456. DOI: 10 . 1109/tim . 2020 . 2987654. [Online]. Available: <https://ieeexplore.ieee.org/document/9064842/>.
- [51] *MD0101 High Voltage Protection T/R Switch with Clamp Diodes*, Microchip Technology, Inc., May 2020. [Online]. Available: <https://ww1.microchip.com/downloads/aemDocuments/documents/APID/ProductDocuments/DataSheets/MD0101-High-Voltage-Protection-TR-Switch-with-Clamp-Diodes-Data-Sheet-20005916A.pdf>.
- [52] H. Ding, D. Yang, M. Qu, *et al.*, “A Pulsed Wave Doppler Ultrasound Blood Flowmeter by PMUTs”, *Journal of Microelectromechanical Systems*, vol. 30, pp. 680–682, 5 October 2021, ISSN: 1941-0158. DOI: 10 . 1109/jmems . 2021 . 3103756. [Online]. Available: <https://ieeexplore.ieee.org/abstract/document/9515180>.
- [53] *ISL55111 Dual, High Speed MOSFET Driver*, Renesas Electronics, April 2021. [Online]. Available: <https://www.renesas.com/us/en/document/dst/isl55110-isl55111-datasheet>.
- [54] M. Winder, A. J. Owczarek, J. Chudek, J. Pilch-Kowalczyk, and J. Baron, “Are We Overdoing It? Changes in Diagnostic Imaging Workload during the Years 2010–2020 including the Impact of the SARS-CoV-2 Pandemic”, *Healthcare*, vol. 9, p. 1557, 11 November 2021, ISSN: 2227-9032. DOI: 10 . 3390/healthcare9111557. [Online]. Available: <https://www.mdpi.com/2227-9032/9/11/1557>.
- [55] “Heart disease facts”. (October 2022), [Online]. Available: <https://www.cdc.gov/heartdisease/facts.htm> (visited on February 23, 2023).
- [56] “Ninja, a small build system with a focus on speed”. (August 2022), [Online]. Available: <https://ninja-build.org/> (visited on February 15, 2023).
- [57] M. Omura, R. Nagaoka, K. Yagi, K. Yoshida, T. Yamaguchi, and H. Hasegawa, “Characterization of blood mimicking fluid with ultrafast ultrasonic and optical image velocimeters”, *Japanese Journal of Applied Physics*, vol. 61, Sg1067, Sg Jul. 2022, Publisher Copyright: © 2022 The Japan Society of Applied Physics., ISSN: 0021-4922. DOI: 10 . 35848/1347-4065/ac4ea9. [Online]. Available: <https://iopscience.iop.org/article/10.35848/1347-4065/ac4ea9>.
- [58] “Zephyr Project Documentation”. (Sep. 2022), [Online]. Available: <https://docs.zephyrproject.org/latest/> (visited on February 15, 2023).
- [59] “Altium Designer - PCB design software”. (February 2023), [Online]. Available: <https://www.altium.com/altium-designer>.
- [60] “CMake Tools - Visual Studio Marketplace”. (February 2023), [Online]. Available: <https://marketplace.visualstudio.com/items?itemName=ms-vscode.cmake-tools> (visited on February 15, 2023).
- [61] L. Li, L. Zhao, R. Hassan, and H. Ren, “Review on Wearable System for Positioning Ultrasound Scanner”, *Machines*, vol. 11, p. 325, 3 February 2023, ISSN: 2075-1702. DOI: 10 . 3390/machines11030325. [Online]. Available: <https://www.mdpi.com/2075-1702/11/3/325>.
- [62] *Sample and hold Sampling Zero-order hold First-order hold Digital-to-analog converter*. [Online]. Available: <https://www.pngwing.com/en/free-png-zueso> (visited on April 10, 2023).

A Source Code

B Simulation Models

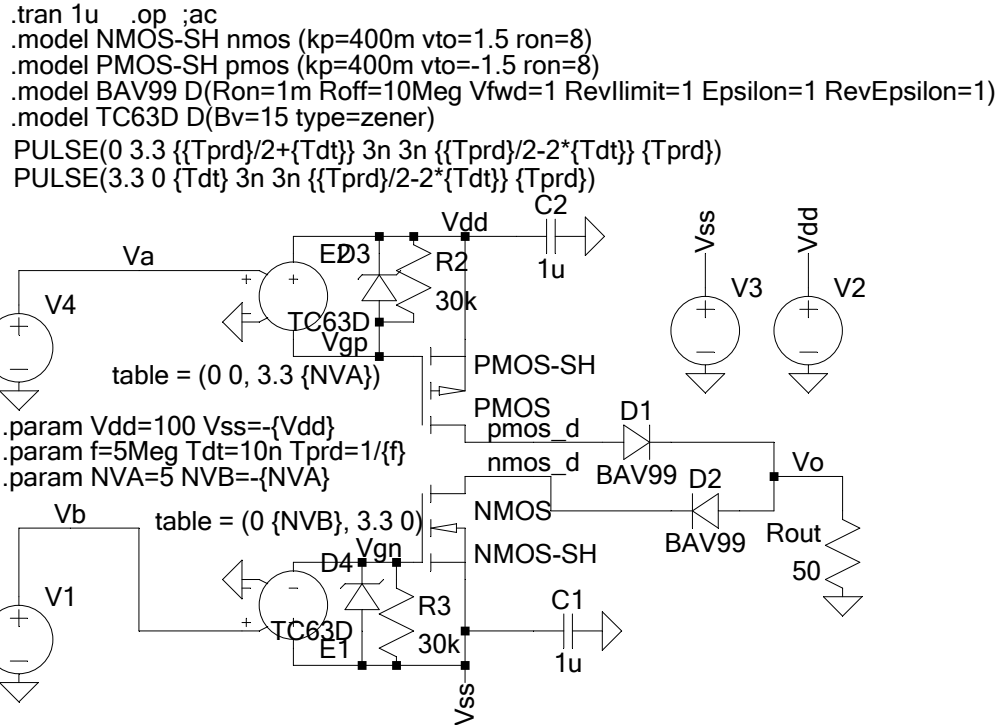


Figure B.1: LTspice model of transmitter

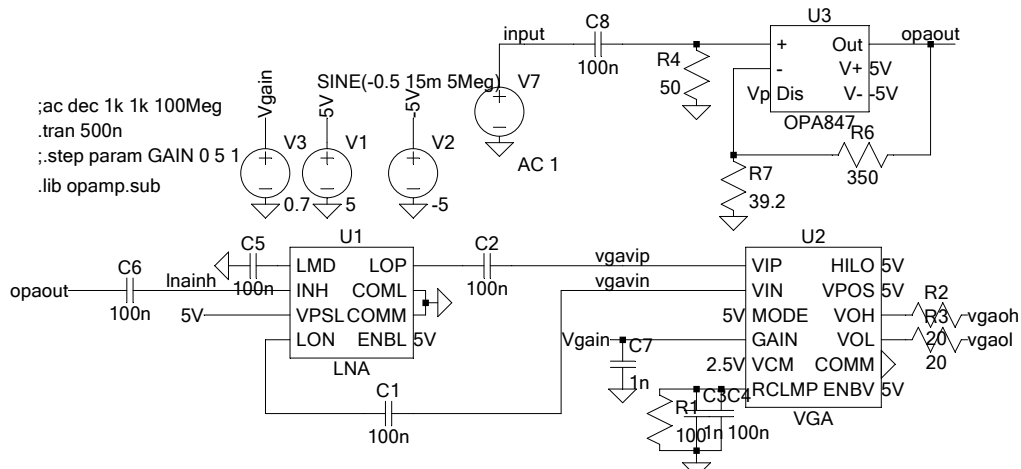


Figure B.2: LTspice model of preamplifier

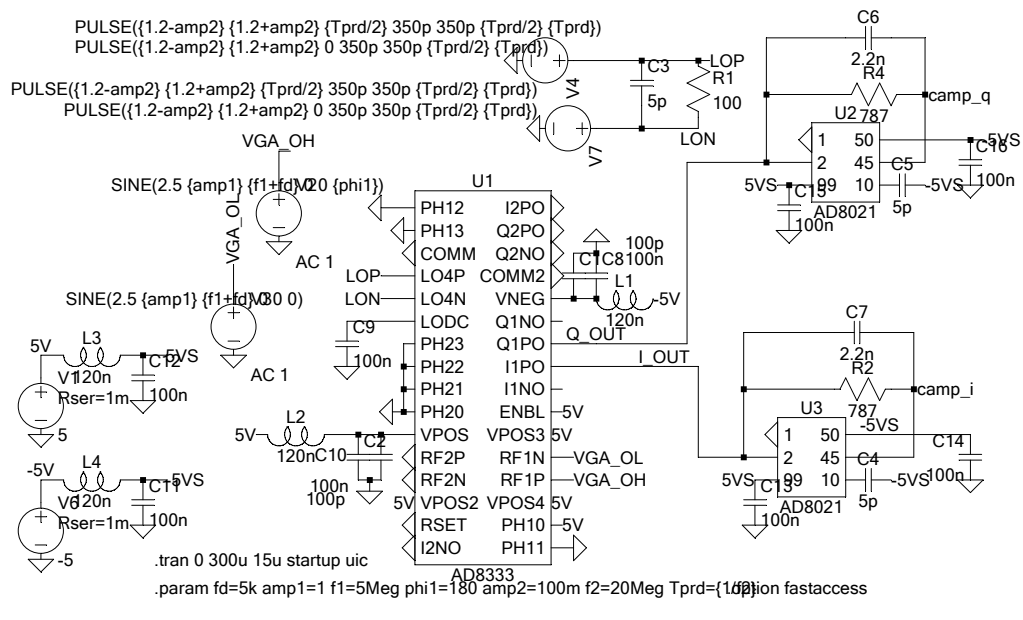


Figure B.3: LTspice model of demodulator

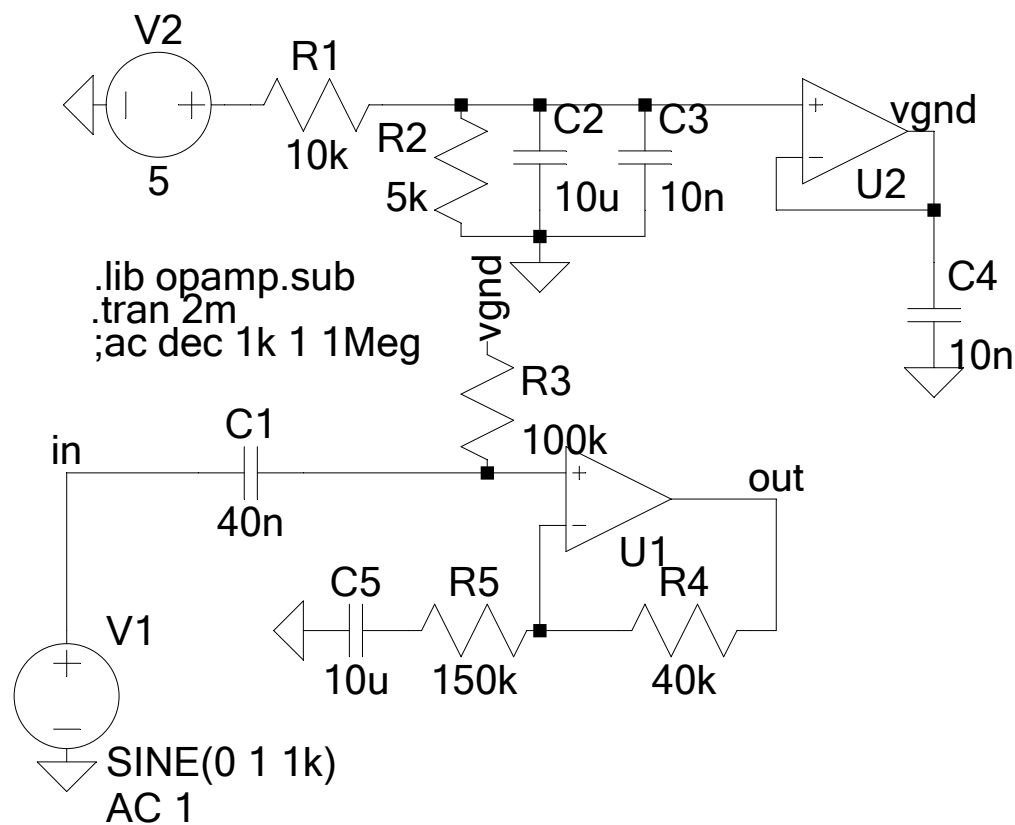


Figure B.4: LTspice model of DC Coupler

C Instruments

Table C.1: List of instruments used for solder work

Function	Manufacturer	Model
Visual inspection microscope	Leica	A60
Manual soldering	Weller	WX2
Heat gun	Thermaltronics	TMT-HA600-2
Solder paste	Chip Quik	SMD291AX250T3
Solder flux	Chip Quik	SMD291NL
Reflow oven	Puhui	T-962A
DMM	Fluke	175

Table C.2: List of instruments used in experiments

Function	Manufacturer	Model
DCPS 1	RIGOL	DP832A 200W
DCPS 2	Keysight	E3631A 80W
Function generator 1	Keysight	33500B
Function generator 2	Tektronix	AFG3102
DMM	Fluke	175
Transducer (PZT)	HAGISONIC	M715-SB-S 204 5 MHz
Transducer (CMUT)	BMM Creation	6ch 3.3 MHz C.F.
RF Amplifier	Tomco	BT00100-AlphaS-CW
Oscilloscope 1	Keysight	DSO-X 2024A
Oscilloscope 2	Tektronix	MSO4054
Physiological simulator	CIRS	Doppler String Phantom 043A
Vector Network Analyzer	Agilent	E5071B ENA Series Network Analyzer